Coordination Chemistry Reviews 443 (2021) 214018

Contents lists available at ScienceDirect

Coordination Chemistry Reviews

journal homepage: www.elsevier.com/locate/ccr

Review

Light-driven catalytic conversion of CO_2 with heterogenized molecular catalysts based on fourth period transition metals

Alessandro Perazio [a,b], Grace Lowe [a], Roberto Gobetto [b], Julien Bonin [a], Marc Robert [a,c,*]

[a] Université de Paris, CNRS, Laboratoire d'Electrochimie Moléculaire (LEM), F-75006 Paris, France
[b] Department of Chemistry, University of Torino, Via P. Giuria 7, 10125 Torino, Italy
[c] Institut Universitaire de France (IUF), F-75005 Paris, France

ARTICLE INFO

Article history:
Received 21 December 2020
Received in revised form 28 April 2021
Accepted 3 May 2021
Available online 25 May 2021

Keywords:
CO_2 reduction
Molecular catalysis
Photochemistry
Solar fuels
Heterogeneous catalysis

ABSTRACT

This review examines recent advances in photocatalytic CO_2 reduction using heterogenized molecular catalysts. The main part of the discussion is focused on the chemistry used to attach catalysts to different supports to produce hybrid materials, and how this effects photocatalytic performance. Examples of hybrid materials used for colloidal dispersions and solid suspensions are presented, including those based on carbon nitride, chalcogenide and perovskite quantum dots, and metal oxides. Some key examples in which this chemistry has been employed to make electrodes and photoelectrodes for photoelectrochemical CO_2 reduction are also presented. In addition, the incorporation of molecular catalysts into ordered, porous frameworks (MOFs and COFs) is discussed because it offers many new and unique chemical pathways for heterogenization. Lastly, an outlook for this field and the potential future impact of these systems on solar fuels research is given.

Contents

1. Introduction . . . 2
2. Heterogenization . . . 3
 2.1. Linkers . . . 4
 2.2. Supporting materials . . . 4
  2.2.1. Carbon-based colloids . . . 4
  2.2.2. Quantum dot-based colloids using metal chalcogenides . . . 4
  2.2.3. Metal oxide-based colloids . . . 5
  2.2.4. Perovskites . . . 5
 2.3. Anchoring strategies . . . 5
  2.3.1. Anchors for carbon-based materials . . . 5
  2.3.2. Anchors for metal oxide-based materials . . . 6
  2.3.3. Anchors for non-oxide semiconductors . . . 7
 2.4. Incorporation into molecular frameworks . . . 7
3. Recent examples of hybrid systems for photocatalytic CO_2 reduction . . . 9
 3.1. Carbon supported systems . . . 9

Abbreviations: AA ascorbic, acid; ACN, acetonitrile; BIH, dimethylphenylbenzimidazoline; BNAH, benzyl-dihydronicotinamide; CB, conduction band; CIGS, copper indium gallium selenium; DLS, dynamic light scattering; DMF, dimethylformamide; DMSO, dimethylsulfoxide; DRIFTS, diffuse reflectance infrared Fourier transform spectroscopy; DSP, dye-sensitized photocatalysis; DSPC, dye-sensitized photocathodes; FTIR, Fourier-transform infrared spectroscopy; MEDA, 2-(dimethylamino)ethanethiol; MES, 2-(N-morpholino)ethanesulfonic acid; MOF, metal–organic framework; MWCNT, multi-walled carbon nanotubes; NC, nanocrystal; NHE, normal hydrogen electrode; PCET, proton-coupled electron transfer; PEC, photoelectrochemical; PL, photoluminescence; PS, photosensitizer, QD, quantum dot; SCE, saturated calomel electrode; SD, sacrificial electron donor; TAS, transient absorption spectroscopy; TEA, triethylamine; TEOA, triethanolamine; TOF, turnover frequency; TON, turnover number; VB, valence bond; XPS, X-ray photoelectron spectroscopy.

* Corresponding author at: Université de Paris, CNRS, Laboratoire d'Electrochimie Moléculaire (LEM), F-75006 Paris, France.
E-mail address: robert@u-paris.fr (M. Robert).

https://doi.org/10.1016/j.ccr.2021.214018
0010-8545/

3.1.1. Carbon nitride . . . 9
3.1.2. Carbon nanotubes . . . 11
3.2. Quantum dot supported systems . . . 11
3.2.1. Cadmium sulfide (CdS) . . . 11
3.2.2. Copper indium sulfide/zinc sulfide ($CuInS_2$/ZnS) . . . 12
3.2.3. Zinc selenide (ZnSe) . . . 13
3.3. Metal oxide scaffolds . . . 14
3.3.1. Titanium oxide (TiO_2) . . . 14
3.3.2. Zirconium oxide (ZrO_2) . . . 15
3.4. Perovskites . . . 15
3.5. Metal-organic frameworks (MOFs) and covalent organic frameworks (COFs) . . . 15
3.5.1. UiO-67 . . . 15
3.5.2. Zif-9 . . . 16
3.5.3. COFs . . . 17
3.6. Photoelectrochemical (PEC) conversion . . . 17
4. Concluding remarks . . . 19
Declaration of Competing Interest . . . 19
Acknowledgements . . . 19
References . . . 19

1. Introduction

Carbon dioxide (CO_2), as the thermodynamic product of combustion, is the most oxidized state of carbon (+4). Therefore, its conversion into useful compounds relies on its reduction. However, the linear CO_2 is a stable molecule and catalysis is required to overcome the energy barriers encountered during its single or multiple electron reduction [1]. The one-electron reduction, leading to its radical anion (Eq. (1)) is indeed highly thermodynamically unfavorable and occurs at very negative potential in aqueous solutions (E^0 = 1.90 V vs. NHE, pH 7) [2]. Then, the reduction with 2, 4, 6 or 8 electrons, with the concomitant transfer of protons, occurs at less negative potentials (Eqs. (2)–(6)) and leads to various C_1 products:

$$CO_2 + e^- \rightarrow CO_2^{\cdot -}, \; E^0 = -1.90 \text{ V} \quad (1)$$

$$CO_2 + 2H^+ + 2e^- \rightarrow HCOOH, \; E^{0'} = -0.61 \text{ V} \quad (2)$$

$$CO_2 + 2H^+ + 2e^- \rightarrow CO + H_2O, \; E^{0'} = -0.53 \text{ V} \quad (3)$$

$$CO_2 + 4H^+ + 4e^- \rightarrow HCHO + H_2O, \; E^{0'} = -0.48 \text{ V} \quad (4)$$

$$CO_2 + 6H^+ + 6e^- \rightarrow CH_3OH + H_2O, \; E^{0'} = -0.38 \text{ V} \quad (5)$$

$$CO_2 + 8H^+ + 8e^- \rightarrow CH_4 + 2H_2O, \; E^{0'} = -0.24 \text{ V} \quad (6)$$

The reduction potential of these reduction reactions gradually shifts to less negative values, *i.e.* to more thermodynamically favorable conditions, but the increase in the number of transferred particles leads to a drastic increase of the reaction kinetic barrier. Selectivity toward a given product is another important factor and a challenge.

When designing new photochemical systems, deciding whether to employ homogeneous or heterogeneous catalysts has a huge impact on the behavior of the system. Solid catalysts such as precious metals and metal oxides are favored for industrial-scale reactions because the catalysts can be easily separated from the reaction mixture. This simplifies both isolation of the products and regeneration and recovery of the catalyst which are economically important processes. Many new photochemical systems are being designed for CO_2 reduction to form fuels and feedstock molecules. The unifying aim behind this focused research effort is to develop industrially relevant processes to replace fossil fuels with solar fuels and feedstock, and to develop an artificial carbon cycle to prevent future accumulation of CO_2. Although solid catalysts show high stability in photochemical systems, they typically give poor selectivity as proton reduction is a competing reaction (kinetically favored over CO_2 reduction) and CO_2 conversion yields a range of different products. In contrast, molecular catalysts may present high selectivity with an acceptable stability and they are easily tunable through ligand design. Molecular catalysts are typically used as homogeneous catalysts in the reaction mixture which means they must be removed from non-gaseous or highly soluble products through extra purification steps. However, it is much easier to investigate and understand catalytic processes in homogeneous systems rather than heterogeneous ones. This is because more *in-situ* spectroscopic techniques are available for homogeneous samples. However, the limited solubility of molecular complexes (so far developed) in aqueous media means they are often used with toxic and volatile organic solvents, and this prevents them being employed in greener and more desirable aqueous environments [3,4].

One strategy to overcome the phase-related issues of solubility and purification for molecular catalysts is to immobilize them on solid supports. This heterogenization can result in many potential benefits. Firstly, the catalyst no longer needs to be soluble in the reaction medium to function. Second, well defined catalytic sites arise on the surface of the material, simplifying the characterization of the species involved in the transformation. More importantly, the catalyst can be readily separated from the reaction mixture which lowers recycling costs. Heterogenization can also be beneficial for electron transfer from the electron source (electrode or molecular partner) to the catalyst. The photoexcited state lifetimes of photosensitizers (PS) are usually shorter than the time it takes for the two components to diffuse towards each other in solution. Therefore, the catalyst cannot collect the multiple electrons required for the reduction in a very efficient way. However, complexes immobilized onto a light absorbing material (or sensitized semiconductor) allow a pre-organization of both the electron donor (PS here) and acceptor (catalyst). Diffusional limitations are removed, and the efficiency of the electron transfer increases. It may also be noted, that the electronic coupling between the orbitals of the catalyst and the conduction band of the light absorbing material may vary with nature of the linkage, and this can give rise to improved performances in optimized conditions. Finally, sup-

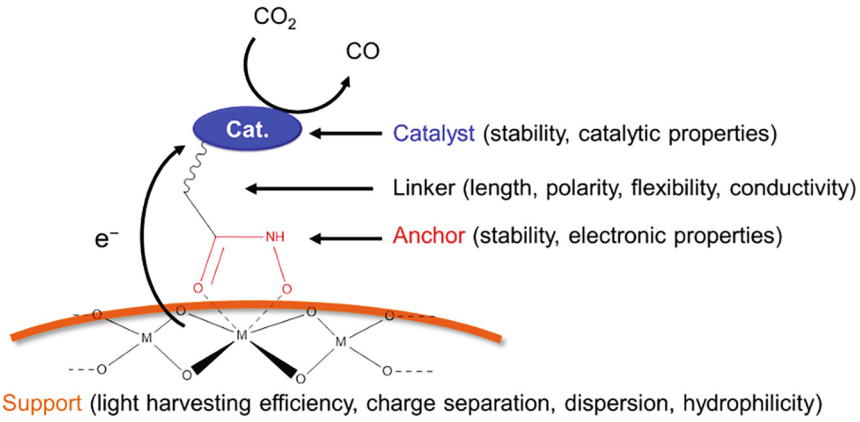

Fig. 1. A scheme of a covalently immobilized molecular catalyst on the surface of a metal oxide support, highlighting the main components of the heterogenized catalyst and which properties they control. Adapted from [6].

ported conditions may offer to molecular catalysts favorable environment (hydrophobicity, local functionality) which could help in outcompeting proton reduction even in aqueous environments [3–5].

This review focuses on the heterogenization of molecular catalysts for light-driven CO_2 reduction, specifically organometallic fourth row transition metal complexes. Different solid support materials are reviewed, from graphitic carbon nitride to chalcogenide quantum dots (QDs), as well as various methods of catalyst attachment. First, examples of photocatalysis with catalyst-modified materials suspended in solutions are discussed, followed by heterogenization of molecular CO_2 reduction catalysts inside metal–organic frameworks (MOFs) and covalent organic frameworks (COFs). Finally, examples of the heterogenization of catalysts onto electrodes and photoelectrodes for photoelectrochemical CO_2 reduction are presented.

2. Heterogenization

Heterogenization of molecular catalysts can be achieved by their immobilization of catalysts onto supports using covalent and non-covalent interactions, or more recently by incorporating the modified catalyst directly into a molecular framework. The catalyst needs to be robust and active under the same experimental conditions as the solid-state material. Properties of the support or framework such as conductivity, morphology, and stability must be carefully considered to obtain an overall efficient catalysis. Usually, the preferred solid scaffolds for photocatalysis are semiconductors: materials that do not allow efficient electronic conduction within their bandgap and may be capable of absorbing light, consequently separating charges (electrons and holes) for a certain amount of time before their recombination. Intuitively, a support with a larger surface area leads to higher catalytic performances, due to the greater number of available sites for the catalyst to be attached. Hence, ideal morphologies for support materials are nanoparticles and porous materials. Various examples of non-covalent attachment, such as electrostatic attraction, Van der Waals interactions and hydrophobic interactions, will be discussed. The method of non-covalent attachment is specific to the system, especially the solvent and support material employed. Catalysts heterogenized using non-covalent interactions are prone to catalyst leaching in most cases, but not all. To prevent leaching, methods for covalent attachment of the catalyst to the support have been developed. They require the chemical modification of the ligand scaffold with an anchoring unit suitable for the support material employed, and different anchoring methods will be discussed in more detail here [6].

To covalently attach a molecular catalyst onto a surface, several different aspects have to be considered to maximize the activity, stability, and selectivity of the system [6]. The chemical structure of the molecule-to-anchor can be divided into three different parts (Fig. 1): (1) a coordination complex that catalyzes the reaction upon reduction; (2) the anchoring group that allows the adsorption of the complex; (3) a linker that ensures connection between the other two components and plays a pivotal role in electron transfer dynamics. This molecule-to-anchor structure can also be used to

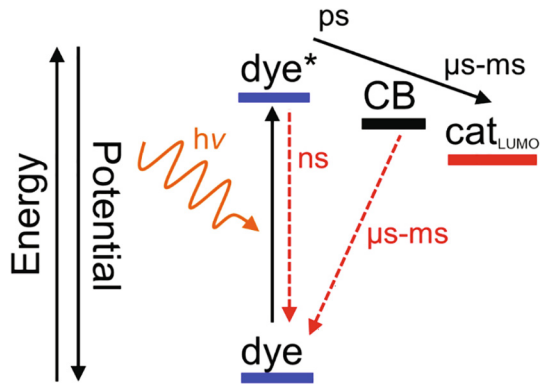

Fig. 2. Electron transfer cascade in the DSP setting. Forward transfer and recombination rates are indicated in black and red, respectively. CB: conduction band of the semiconductor. Adapted from [9].

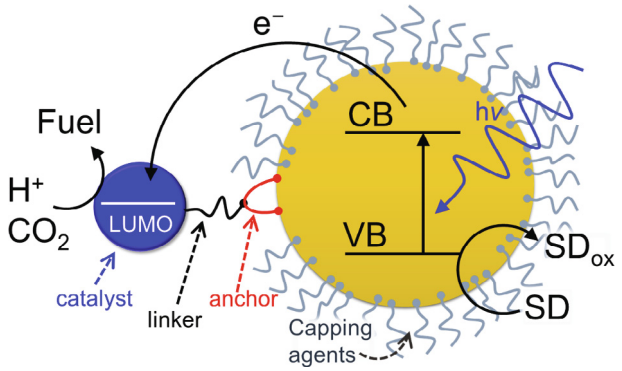

Fig. 3. Representation of CO_2 reduction with a catalyst (blue) attached to a QD (yellow) where the latter acts as a photosensitizer and is regenerated by a SD. Adapted from [10].

add anchoring groups such as pyrenes, or cationic moieties for non-covalent attachment strategies.

2.1. Linkers

In order to attach the anchoring group to the catalyst, a linker moiety is often introduced between the two components [6]. The linker is usually attached to the catalyst through covalent modification of at least one of the ligands. Since any modification to the ligand structure can lead to changes in steric and electronic properties of the catalyst, the choice of the linker is a crucial step. The covalent modification may induce dramatic changes in the overpotential required for the reduction, or the ligand flexibility may also be affected changing the molecule's ability to generate catalysis-favorable conformations. Moreover, electron transfer kinetics between the catalyst and the surface are heavily affected by the length, orientation, and chemical nature of the linker.

2.2. Supporting materials

To have an efficient photocatalytic system, the solid material that supports the catalyst (and potentially a photosensitizing dye) should have some general characteristics such as a high surface area, simple functionalization pathways, appropriate electronic band structure, and in the case of a photosensitizer, efficient light harvesting [6]. Colloidal dispersions are made of particles ranging between 1 and 1000 nm (between 1 and 100 nm they are called nanoparticles) and as a result provide a large surface area [7,8]. Hence colloidal dispersions of materials such as semiconductors are ideal catalyst supports for employing heterogenized catalysts in photocatalytic reactions.

Semiconducting particles can be used as a scaffold to carry out dye-sensitized photocatalysis (DSP, Fig. 2) [9]. While providing a support for the catalyst and the dye (or PS), they also act as an electron mediator between these two moieties. The role of the semiconductor is to transfer electrons from the excited state of the dye to the catalyst, thus properties like charge mobility and electron injection rates have to be carefully considered. Another critical feature for electron transfer is the energy separating the valence band (VB) and the conduction band (CB) of the semiconductor, *i.e.* the bandgap energy. The most stable semiconductors are the ones with a wide bandgap (*e.g.* metal oxides) that can only utilize UV light to generate the electron-hole (e^-—h^+) couples, while narrow bandgap semiconductors which can also employ visible light, are often unstable as they suffer from photo-corrosion in aqueous environments. However, in DSP the width of the bandgap is not important because the light absorption occurs at the dye. For CO_2 reduction, only the CB value is relevant and it must have a reduction potential less negative than that of the dye to facilitate electron transfer. This is a great advantage as it allows more stable wide bandgap semiconductors to be used as support materials.

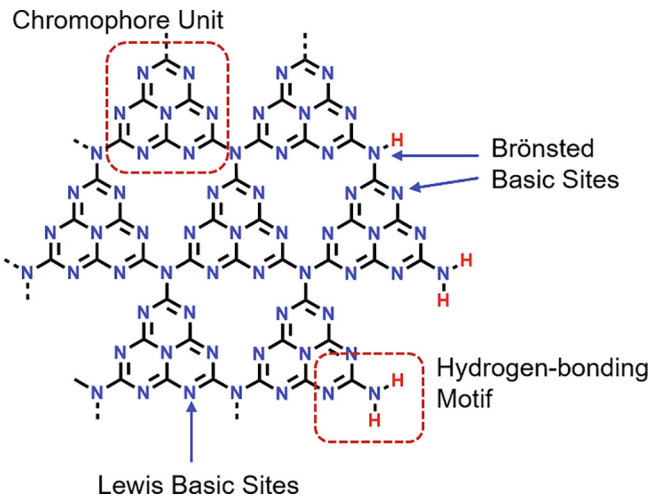

Fig. 4. Structure of tris-S-triazine, one of the possible g-C_3N_4 allotropes, indicating basic sites and hydrogen bonding motifs in the structure. Adapted from [20].

An alternative way in which semiconductor nanoparticles are employed in photocatalysis is the quantum dot (QD) system (Fig. 3) [10]. A QD is a single nanocrystal of semiconductor with an electronic wave function that is quantum confined in all three dimensions. This creates a peculiar electronic structure different from that of bulk solids and simple molecules.

The unique properties of QDs arise also from the quantum-confined nature of the energy carriers (namely electrons) and the very high ratio between surface area and volume. Semiconductor QDs are able to generate e^-—h^+ pairs upon irradiation and then act as electron (for reductive reactions) or hole (for oxidative reactions) donors. Consequently, in this type of system there is no need to use a dye since the QD serves as the PS moiety as well as the catalyst support. Catalytic ability of QDs are greatly improved when associated with a co-catalyst, which can be a metal nanoparticle, a metal ion, a metal oxide or a metal complex [11–13]. Unlike bulk materials, most QD atoms are surface atoms, so QD properties are highly sensitive to surface properties. They are commonly sensitive to water, oxygen, and UV-irradiation, so various strategies were developed to enhance their stability through suitable design of the shell, ligand and overcoating. Such protective strategies are also potentially beneficial for further catalyst anchoring [14]. Moreover, QDs can continuously absorb multiple photons even after electrons and holes have been accumulated, which is a great advantage for multielectronic reactions, such as those involved in CO_2 reduction. The most suitable materials for colloidal photocatalysis are discussed below.

2.2.1. Carbon-based colloids

Colloidal dispersions of carbon-based materials are often based on carbon atoms and heteroatoms in a sp^2 configuration with planar organization that leads to conjugation [6]. Materials such as carbon nitrides [15], graphene [16], carbon nanodots [17] and organic polymers [18], can also act as light-harvesters. Their non-toxic nature [19], low cost, Earth-abundant elements, and scalability makes carbon colloidal dispersions desirable materials to employ in a photocatalytic system.

Graphitic carbon nitride (g-C_3N_4) is a metal-free semiconductor which is insoluble in most solvents and inert against most acids and bases [20]. It is made through thermal polymerization of precursors such as cyanamide, dicyanamide, or melamine, to make highly ordered structures. The tris-*S*-triazine allotrope is shown in Fig. 4 [20]. The band gap of g-C_3N_4 is in the visible range so that it can also act as a photosensitizer, as well as a catalyst support. g-C_3N_4 has peculiar surface characteristics such as combinations of Lewis and Brönsted basic nitrogen sites [21]. These surface functionalities are useful for covalent attachment of molecules and they have been shown to interact with CO_2 and CO [20,22].

2.2.2. Quantum dot-based colloids using metal chalcogenides

Soluble metal chalcogenide nanocrystals (QDs) are excellent photosensitizers. They are commonly made of a chalcogen atom (S, Se, and Te) and metals like Cd, Zn, In, or Ga and the value of their conduction band and valence band can be controlled by particle size. Moreover, they have large extinction coefficients and a high degree of tunability of both their cores and surfaces, with the latter being the most interesting [23]. As a matter of fact, for these nanocrystals (diameter around 5 nm) the ratio of (potential) catalytically active surface area to volume increases by a factor of

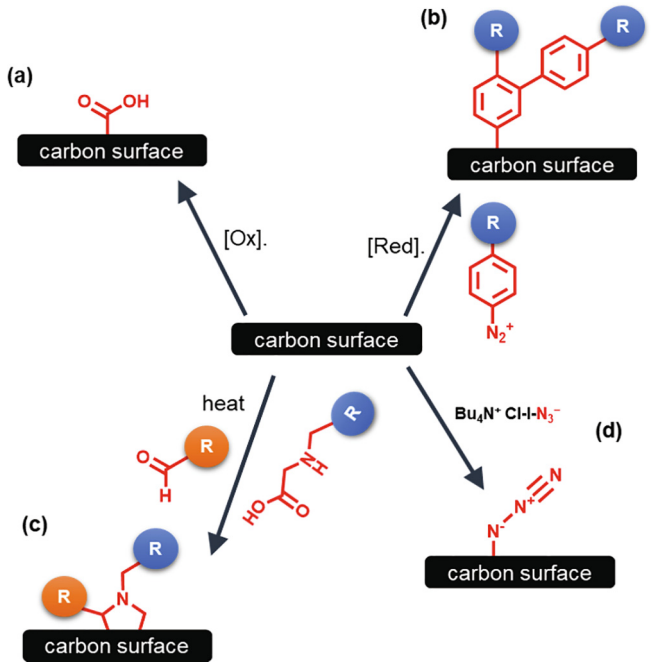

Fig. 5. Examples of commonly used methods to covalently bind anchoring groups onto carbon surfaces: (a) oxidation to introduce C-O functionalities; (b) reduction of diazonium salts; (c) 1,3-dipolar cycloaddition of azomethine ylides to form pyrrolidine units; (d) introduction of azide groups. Adapted from [6].

~10^6 when compared to millimeter-sized particles [23]. While common homogeneous catalysts have just one or two sites to bind the substrate, QDs have tens to hundreds of binding sites that can in principle be functionalized with molecular catalysts. It is also important to maximize the electron transfer rate from the quantum dot to the chemisorbed catalyst because faster redox processes prevent the accumulation of side products and increase the selectivity of the reaction. However, metal chalcogenides QDs are not perfect as they have issues such as toxic constituent elements (*e.g.* cadmium), and surface defects that lead to recombination. These issues must be addressed to incorporate such QDs into benign and scalable photocatalytic systems.

2.2.3. Metal oxide-based colloids

Most common metal oxides are comprised of relatively inexpensive and Earth-abundant materials, so they are good candidates for support materials in industrial scale reactions [24]. Oxides like TiO_2, Al_2O_3, ZrO_2 and SiO_2 have wide bandgaps which do not allow them to use visible light to generate the electron-hole pair. For this reason, they are suitable materials for the aforementioned DSP. They can be easily functionalized with both catalysts and dyes and they show a good stability under catalytic conditions. Moreover, thanks to their relative chemical inertness compared to the other materials, unwanted side-reactions are often prevented with metal oxide supports [25,26].

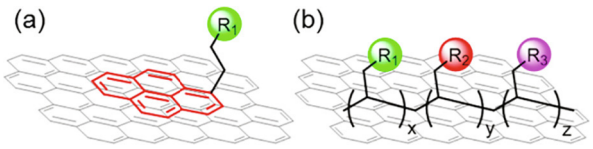

Fig. 6. Representation of noncovalent modification of graphitic-like surfaces with (a) compounds bearing a pyrene moiety and (b) hydrophobic polymeric chains. Reproduced with permission from [6].

2.2.4. Perovskites

Halide perovskite nanocrystals (NCs) recently emerged as great alternatives to well-established chalcogenide NCs [27]. In addition to already mentioned advantageous features of semiconductor NCs (*e.g.* high molar extinction coefficient, broader absorption range in the visible, convenient synthesis and plethora of surface sites) [13], perovskite NCs also have relatively low non-radiative recombination rates, tunable chemical composition and structure through post-synthetic transformations [28]. As a consequence, perovskite NCs are on the short list of the most promising materials for designing highly efficient photocatalytic systems, for example when coupled to QDs [29,30], MOFs [31] or a molecular unit [32].

2.3. Anchoring strategies

The reaction conditions used to anchor a catalyst onto a surface are critical, as they must be compatible with the chemical stability of the catalyst. Covalent grafting provides a more stable link but the approach usually requires harsher conditions than non-covalent strategies [6]. The anchoring group itself inevitably affects the electronic properties of the materials, and has an important role in modulating the electron transfer between the catalyst and the surface. In fact, its presence may generate dipoles at the surface, break orbital overlap, release protons or block the surface from the solvent, and all these effects have an influence in the electronic characteristic of the support.

2.3.1. Anchors for carbon-based materials

A covalent grafting to a carbon support is commonly achieved through two steps; first the sp^2 surface is functionalized with the anchoring group, and then in a second step the immobilized anchoring groups react with a (modified) ligand of the molecular catalyst [6]. Some of the most useful reactive groups to employ as anchors are carbon–oxygen functionalities like carboxylic acids, ketones, and quinones. Carbon-nitrogen functionalities such as aryl diazonioum compounds, pyrrolidine units, and azide groups can also be used as anchoring groups (Fig. 5) [6].

Anchoring groups containing the C=O moiety can be generated by applying oxidizing conditions to the carbon support [33]. The complexes may then be anchored to the surface through the carboxylic acid functionalities. For instance, through the formation of ester or amide bonds (Fig. 5(a)). However, oxidation is not easy to control and can lead to degradation of the material. A less drastic way to modify carbon surfaces is the reduction of aryl diazonium compounds [34], which bear the group meant to react with the catalyst on the aromatic ring(s) (Fig. 5(b)). The reduction forms radical species that are able to cover the sp^2 carbon surface very efficiently [35]. A good method to introduce a functionality that bears two different (or equal) grafting groups on a graphitic-like support is through the condensation of an α-amino acid and an aldehyde [36]. The resulting azomethine ylide undergoes a 1,3-dipolar cycloaddition to yield a pyrrolidine unit at the surface of the material (Fig. 5(c)). To prepare carbon surfaces modified with azide groups (Fig. 5(d)), iodine azide (IN_3) is used to perform the Hassner reaction, which introduces the azide functional groups at the graphitic edges [37]. Other examples in the literature involve the addition of carbenes or nitrenes, cyclopropanation, and Diels-Alder addition.

Noncovalent strategies can also be employed to anchor metal complexes to carbon surfaces. By avoiding a direct chemical link to the support, a noncovalent interaction prevents the alterations of the surface electronic properties that may arise as a result of the disruption of π-conjugation when forming a covalent link. The compounds used in noncovalent anchoring are usually aromatic molecules or polymers, which provide the anchoring by means of π-π stacking or hydrophobic interactions [38]. Pyrene

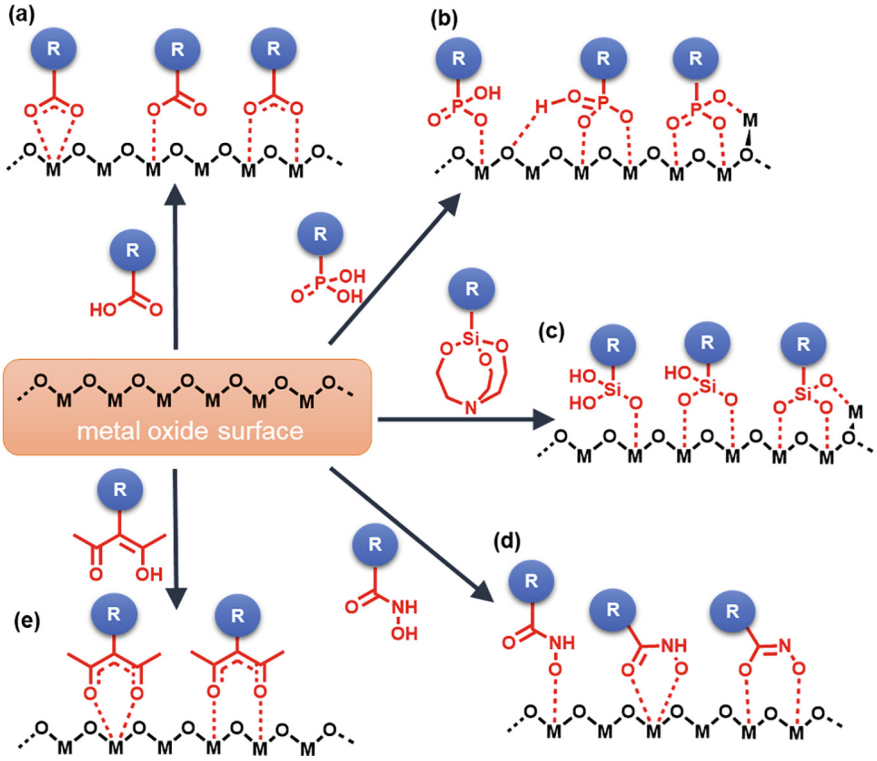

Fig. 7. Surface binding modes of different anchors onto metal oxide materials: (a) carboxylates, (b) phosphonates, (c) silatranes, (d) hydroxamates and (e) acetylacetonates. Adapted from [6].

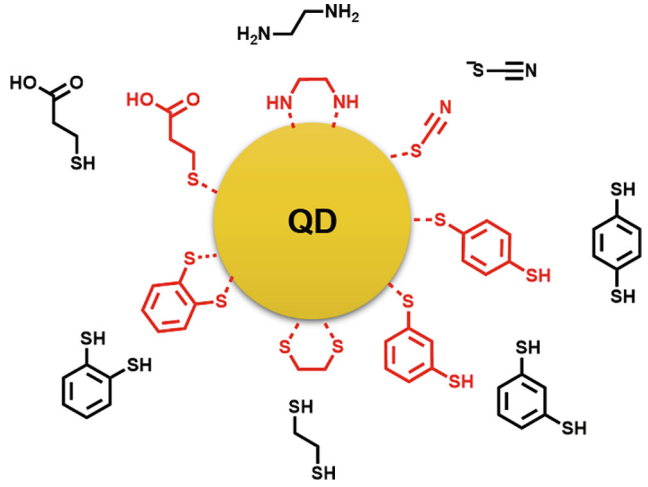

Fig. 8. Examples of suitable surface ligands for photocatalytic applications on a chalcogenide quantum dot. Adapted from [6].

is a good choice among the polycyclic aromatic derivatives as it provides a strong interaction with the support and tunable catalyst loading (Fig. 6(a)) [39]. Meanwhile, polymers have the advantage of carrying several functional groups that will later react with the catalysts (Fig. 6(b)) [6].

2.3.2. Anchors for metal oxide-based materials

Metal oxide are an attractive platform for the immobilization of molecular complexes and PSs, as they are easily accessible, thermodynamically stable, and they can also be prepared in a wide variety of nanometer-sized structures. The chemistry of MOx surfaces is governed by the presence of hydroxyl groups which can be used as grafting functionalities, and by the Lewis acidity/basicity of the surface. Typical anchoring groups are carboxylates, phosphonates, silatranes, hydroxamates, and acetylacetonates because they often meet the requirements regarding stability and electronic properties needed for efficient catalysis [40]. Carboxylates are widely used as anchors for metal oxides materials [41]. They are easily accessible as they have a lot of commercially available precursors and they form an ester-type linkage with the hydroxyl groups on the MOx surface, which can bind in various modes as depicted in Fig. 7(a). However, carboxylic residues are prone to dissociate from the support when exposed to neutral and alkaline aqueous environments. To overcome this issue, phosphonic acids became popular as a more stable alternative to carboxylic acid derivatives [42]. The reason for the improved binding strength towards the surface arise from the dianionic nature of the phosphonate ions and also from their ability to coordinate the surface in a tridentate fashion (Fig. 7(b)) [42]. Phosphonate groups tolerate a wider pH window compared to the carboxylic analogues, but they also suffer from hydrolysis in basic conditions. Silatrane (triethanolamine-protected trialkoxysilanes) groups are convenient for linking molecular compounds to metal oxides through siloxyl bonds [41]. They are believed to be deprotected *via* nucleophilic attack of the surface hydroxyl groups at the silicon, thus forming the covalent anchor-support link. The resulting silicon-oxygen bond is reported to be significantly less liable than the ester bond formed by carboxylic and phosphonic acids (Fig. 7(c)). Hydroxamates constitute another anchoring strategy (Fig. 7(d)) [43]. They are interesting as they can form more stable adducts than carboxylates with the metal oxide surface, and they allow a faster interfacial electron transfer between the dye and the catalyst than other grafting groups such as phosphonates [44]. Lastly, acetylacetonates allow the formations of strong surface adducts, stable even in aqueous conditions, thanks to their affinity with the metals commonly present within the oxide supports (Fig. 6 (e)) [45].

2.3.3. Anchors for non-oxide semiconductors

As an alternative to carbon- and oxide-based supports, molecular catalysts can also be immobilized on chalcogenide QDs. The electronic properties of these QDs can be modulated through adjustment of their surface capping ligands [46]. Commonly reported compounds for anchoring catalysts to chalcogenides are bidentate aliphatic and aromatic thiols, bidentate primary amines, carboxylic acids and thiocyanate ions (Fig. 8). These functionalities are able to bind to the surface and provide anchoring groups to attach molecular catalysts. The method is comparable to the two-step method used for graphitic-like carbon, and metal oxide materials. The various anchoring groups influence properties of the resulting systems in different ways, such as carrier mobility inside the QD (*e.g.* by decreasing the ligand length the mobility increases exponentially) and the QD-ligand surface dipole, which depends on the charge separation of the ligand.

2.4. Incorporation into molecular frameworks

Instead of attaching catalysts onto solid supports, they can also be immobilized in porous organic frameworks. MOFs and COFs are extended ordered structures with well-defined pores, and often beneficial opto-electronic properties. MOFs are constructed from the coordination of large bidentate or multidentate ligands to metal or metal oxide clusters. The combination of different organic ligands and inorganic corner units with different coordination numbers and geometries can be used to generate a wide range of porous structures that interact with gases in interesting ways. In most cases catalysts are heterogenized onto MOFs using the same catalyst-to-anchor structure as we have just discussed. However, the MOF bridging ligands often also must be modified to connect to the anchoring group. Some examples take advantage of existing coordination sites in MOF bridging ligands to coordinate the catalyst directly onto the MOF. This effectively replaces one of the original catalyst ligands with the MOF. Both of these methods conveniently place the catalysts within the MOF pores, however, we also discuss an example where a catalytic metal center has been used as corner unit to coordinate the bridging ligand and make a MOF framework [47]. The heterogenization of catalysts within MOFs has recently been reviewed, including polyoxometalates [48]. However, we will highlight a few key examples of 4th row transition metal organometallic catalysts (see sub-sections 3.5.1 and 3.5.2).

COFs are entirely organic covalent networks. These highly ordered crystalline polymers typically achieve well-defined pore

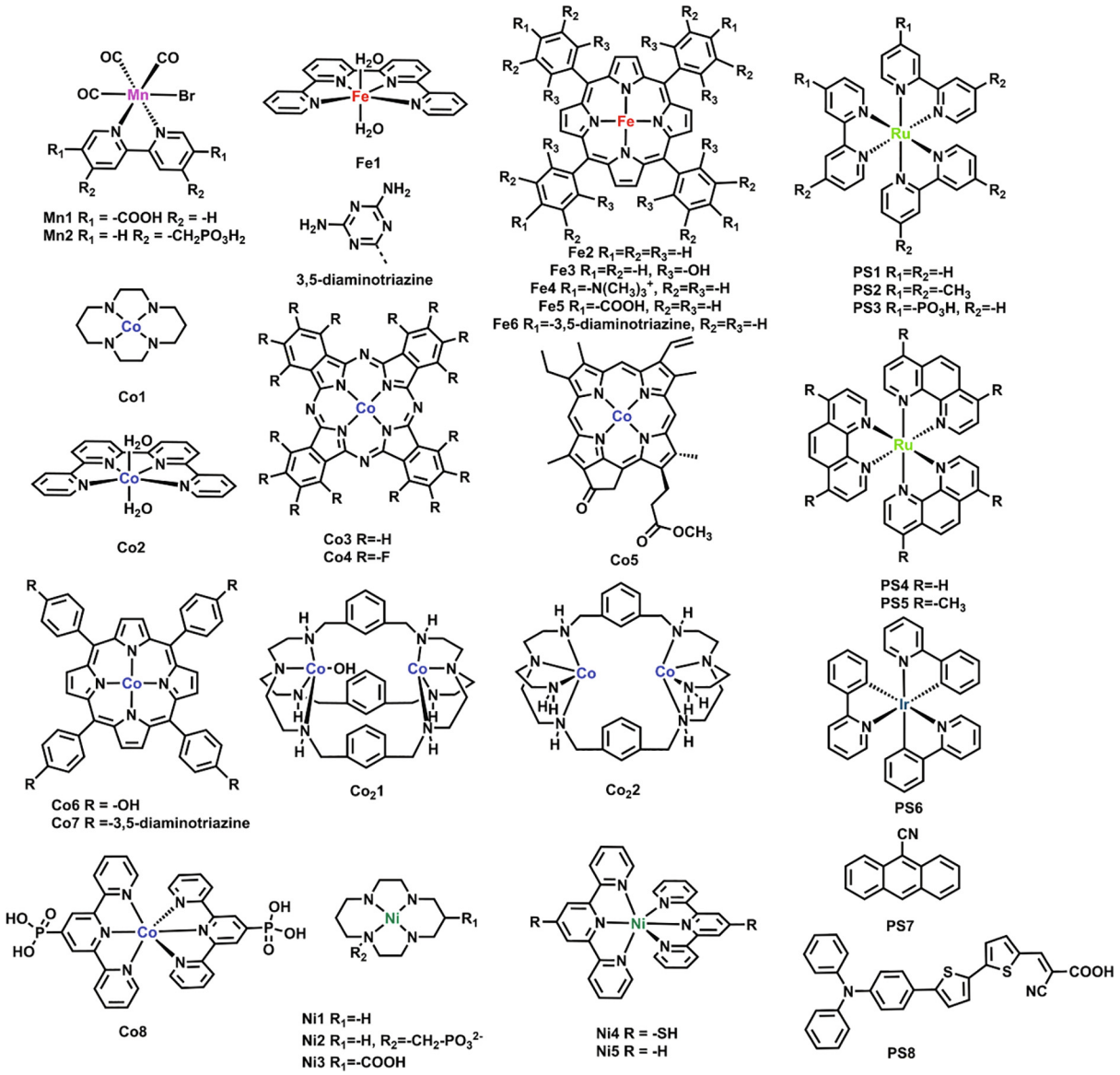

Chart 1. Molecular structures of the catalysts and sensitizers described in this review.

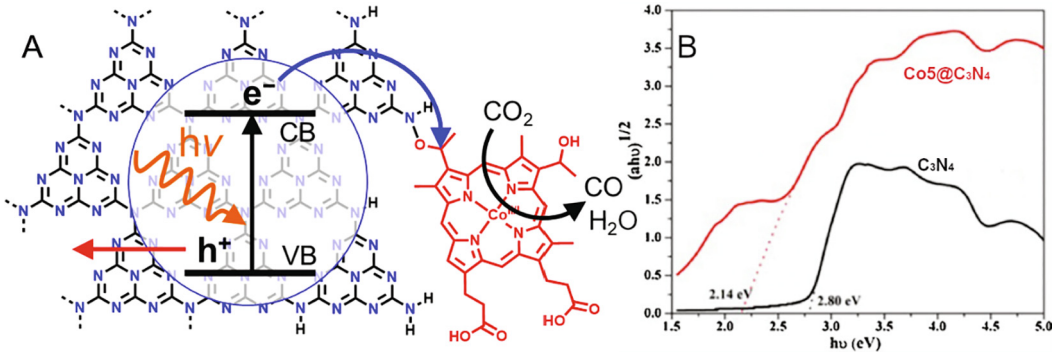

Fig. 9. A. Proposed mechanism for CO_2 reduction with the **Co5@C_3N_4** system. **B.** Plot of Kubelka-Munk function *vs.* exciting light energy. Bandgap energy values for **Co5@C_3N_4** and C_3N_4 extrapolated from the absorption edges. Reproduced from [52].

Table 1
Hybrid systems for photocatalytic CO_2 reduction; nr = not reported.

Entry	Cat	Support	SD	Conditions	Main products (TON, Φ)	Selectivity	Refs.
1	**Co5**	g-C_3N_4	TEOA	ACN λ > 420 nm	CO (<1) H_2	80% (CO)	[52]
2	**Co7**	g-C_3N_4	TEOA	ACN λ > 400 nm, 5 h	CO (200 μmol g^{-1})	nr	[54]
3	**Fe5**	g-C_3N_4	TEOA	ACN/H_2O λ > 420 nm, 6 h	CO (5.7) CH_4(trace)	98% (CO)	[55]
4	**Fe5**	g-C_3N_4-$C_{0.07}$	TEOA	ACN/H2O (3:1) 400 < λ < 780 nm, 6 h	CO (24.9) H_2(55) CH_4(trace)	31% (CO)	[56]
5	**Co3**	mpg-C_3N_4	TEOA	ACN λ > 300 nm, 48 h	CO (84, 0.03%) H_2	85% (CO)	[57]
6	**Co2**	mpg-C_3N_4	BIH	ACN λ > 400 nm, 24 h	CO (128) H_2	98% (CO)	[58]
7	**Fe1**	mpg-C_3N_4	TEOA	ACN λ > 400 nm, 17 h	CO (155, 4.2%)	97% (CO)	[59]
8	**Co5**	MWCNT-PS14	TEOA	ACN/H_2O λ > 420 nm, 20 h	CO (501) H_2 (209)	CO/H_2 = 2.4	[60]
9	**Ni4**	CdS	TEOA	H_2O λ > 400 nm, 8 h	CO (20) H_2	> 90% (CO)	[61]
10	**$Co_2$2**	CdS	TEOA	H_2O/$NaHCO_3$ λ > 420 nm, 120 h	CO (1380) H_2, CH_4	95% (CO)	[62]
11	**Fe2**	$CuInS_2$/ZnS	TMPD	DMSO λ = 450 nm, 40 h	CO (55, 0.01%) H_2	84% (CO)	[63]
12	**Fe4**	$CuInS_2$/ZnS	TEOA	H_2O λ = 450 nm, 30 h	CO (450, 0.025%) H_2	99% (CO)	[64]
13	**Ni2**	ZnSe	AA	H_2O λ > 400 nm, 20 h	CO (283) H_2	33.8% (CO)	[65]
14	**Co1**	TiO_2	TEOA	H_2O UV Hg lamp, 4 h	CO (20) H_2	CO/H_2 = 1	[66]
15	**Mn1**	TiO_2-PS8	BIH	DMF λ > 400 nm, 26 h	$HCOO^-$ (60) CO (<1) (at low **Mn1** loading)	nr	[67]
16	**COD-H**	TiO_2-PS15	MES	H_2O λ > 420 nm, 4 h	CO (2000, 0.07%)	100% (CO)	[68]
17	**Ni2**	ZrO_2-PS15	AA	H_2O λ > 375 nm, 7 h	H_2 CO (4.8)	H_2/CO = 4.15	[69]
18	**Ni5**	$CsPbBr_3$	H_2O	Ethyl acetate/water λ > 400 nm, 4 h	CO, CH_4	CO/CH_4 = 6.67	[32]
19	**Mn2**	UiO-67	BNAH	DMF/TEOA/PS11 λ_{max} = 470 nm, 18 h	$HCOO^-$ (110, 6.74%) CO, H_2	96% ($HCOO^-$)	[70]
20	**Fe5**	MAPbI3@PCN-221(Fe0.2)	H_2O	ethylacetate/H_2O 300 W Xe, 80 h	CH_4 (1.05 mmol g^{-1}) CO (0.52 mmol g^{-1})	66% (CH_4)	[31]
21	**Co-ZIF-9**	–	TEOA	ACN/H_2O/PS1 λ > 420 nm, 2.5 h	CO + H_2 (450)	nr	[47]
22	**Co-DQTP COF**	–	TEOA	ACN/PS1 λ ≥ 420 nm, 4 h	CO (2.18)	59.4% (CO)	[71]
23	**Co-DQTP COF**	–	TEOA	DMA/PS1 λ ≥ 420 nm, 4 h	HCOOH (0.947 mmol) CO(trace)	nr	[71]

structure through covalent attachment of bridging groups to organic groups with multiple points of attachment, such as melamine. Coordination sites and anchoring groups, or even entire catalysts, are usually introduced by modifying the monomers of the COF prior to polymerization. However, the components must be stable at the high temperatures used to form the resulting COF.

Recently advancements in pore functionalization allow anchoring groups and catalysts to be attached to different COFs post-polymerization [49,50]. However, at the time of writing this has not yet been carried out for fourth row transition metal CO_2 reduction catalysts (see sub-section 3.5.3).

3. Recent examples of hybrid systems for photocatalytic CO_2 reduction

In 1979 Inoue *et al.* published a pioneering work that described the photocatalytic reduction of CO_2 to compounds like formaldehyde and methanol. These experiments involved only photosensitive semiconductor powders suspended in water, without the addition of any metal complex [51]. Since then, semiconductor-mediated CO_2 photoconversion driven by solar energy has been much investigated as a means to achieve this difficult yet promising transformation [21].

In the following sections, literature examples of photocatalytic hybrid systems involving earth-abundant transition metal complexes anchored to various (photoactive) supports are presented.

3.1. Carbon supported systems

3.1.1. Carbon nitride

Ye and coworkers efficiently immobilized a cobalt porphyrin (**Co5**, Chart 1) on g-C_3N_4 oligomers with a covalent linkage [52]. The **Co5@C_3N_4** hybrid was obtained through condensation of pendant amino groups on the carbon nitride and porphyrin ketonic groups. The attachment of the catalyst was confirmed by Fourier transform infrared spectroscopy (FTIR) and X-ray photoelectron spectroscopy (XPS), alongside other analyses. Plotting the transformed Kubelka-Munk function (which provides the conversion of reflectance data into a parameter which is proportional to the rate between absorption coefficient and scattering) *vs.* the light energy (Fig. 9) shows a red shift in the absorption edge of **Co5@C_3N_4** compared with that of unmodified g-C_3N_4. This demonstrates the narrower bandgap of the hybrid (2.14 eV) compared to pure carbon nitride (2.80 eV). Similarly, the **Co5@C_3N_4** conduction band has a value of −0.78 V *vs.* NHE, which is less negative than that of the unmodified semiconductor (−0.98 V *vs.* NHE), and this is due to the covalent attachment of the porphyrin [52]. The narrow bandgap allows the hybrid to absorb a greater fraction of visible light which was confirmed by UV–Vis absorption measurements. The system was tested under reactive conditions using TEOA as a SD and 420–800 nm wavelength visible light irradiation. A CO production rate of 17 μmol g^{-1} h^{-1} over four consecutive experiments, **Co5@C_3N_4** outperforms a simple mix of the support and catalyst (7.2 μmol g^{-1} h^{-1}). The selectivity of photocatalytic CO_2 reduction with the hybrid is around 80% for CO, and the quantum yield for CO is 0.8% under irradiation at 420 nm (Table 1, entry 1). Fig. 9 illustrates the global process for CO_2-to-CO reduction. Further investigations found that the TON_{CO} with respect to the cobalt porphyrin in this system was <1 [53].

Very recently, porphyrins **Co7** and **Fe6** (Chart 1) modified with triazine anchoring units were co-polymerised with urea to make covalently functionalized g-C_3N_4 hybrids, **Co7@C_3N_4** and **Fe6@C_3N_4** [54]. Urea was specifically chosen as the monomer because of its lower melting point; urea melted and dissolved the porphyrins before polymerizing to form the g-C_3N_4 hybrid material which allowed the co-polymerisation and dispersion of the porphyrins within the polymer. TONs (defined as per mole of catalyst) were not reported for these hybrid materials, however, 5 h illumination (λ > 400 nm) of **Co7@C_3N_4** in ACN/TEOA produced 200 μmol g^{-1}, while **Fe6@C_3N_4** and g-C_3N_4 produced <25 μmol g^{-1} of CO under the same conditions (Table 1, entry 2). A Ni-analogue was also produced but with reactivity similar to **Fe6@C_3N_4**. Covalent functionalization using co-polymerisation with triazine anchoring groups and more conjugated porphyrins led to improved performance, extended absorption range, and polymers with larger surface areas; the surface area measured by N_2 adsorption was 188 m^2 g^{-1} for **Co7@C_3N_4** and 58 m^2 g^{-1} for g-C_3N_4. This example highlights the importance of anchoring group selection.

After the first report of covalently immobilized cobalt porphyrins on g-C_3N_4, the catalyst [Fe^{III}(TCPP)Cl] (**Fe5**, Chart 1; TCPP = tetra(4-carboxyphenyl)porphyrin)) was bound to the surface of g-C_3N_4 nanosheets by strong noncovalent interactions to give **Fe5@C_3N_4** [55]. The carboxylic acid groups interact with the pendant amino groups of the semiconductor through hydrogen bonding, while π-π stacking connects the aromatic rings of the two moieties. The existence of these interactions was supported by FTIR analysis. The spectra showed distinct peaks that indicate non-covalent bonding between the colloid and the molecular complex. These strong non-covalent interactions allowed effective charge transfer between the two components. Under irradiation (λ > 420–780 nm for 6 h) the hybrid was able to produce CO with a TON of 5.7 (rate of 1.09 mmol g^{-1} h^{-1}) and 98% selectivity, along with trace amounts of CH_4 (Table 1, entry 3). The was a marked improvement over the first immobilized Co-porphyrin system.

An analogue of the **Fe5** catalyst with hydrogens in place of the carboxylic acid moieties, **Fe2**, was studied in the same system to determine the effect of the carboxylic groups. The system exhibited very low activity towards CO_2 reduction when **Fe2** was used instead of **Fe5**. This is likely and mainly because the COOH groups strengthen the interaction with g-C_3N_4 through H-bonding. In addition, their electron-withdrawing nature makes the reduction potential of the Fe center less negative compared to that of **Fe2** and hence the FeTCPP is more prone to accept the photoexcited electrons which may benefit the catalysis even if the intrinsic activity of **Fe5** is lower than that of **Fe2**. Effective electron transfer from the light absorber g-C_3N_4 to the catalyst was confirmed by photoluminescence (PL) measurements. The carbon nitride emission signal can be quenched by the incorporation of **Fe5** on its surface, which indicates a decreased recombination of charge carriers within the semiconductor, meaning that electrons are flowing from the support to the anchored catalyst. Another group enhanced the photocatalytic yield of **Fe5@C_3N_4** by doping the C_3N_4 with carbon quantum dots (CDs) to make **Fe5@C_3N_4/CD** [56]. Doping the C_3N_4 in this way could increase the TON_{CO} from 6.7 to 24.9 (Table 1, entry 4). However, doping the material with too many CDs decreased the yield and increased H_2 selectivity. Doping the support with trace amounts of CDs appears to improve charge separation and transfer to **Fe5**. This example highlights the importance of the electronic properties of the support material in the heterogenization of catalysts.

Graphitic carbon nitride can be organized into a mesoporous structure (mpg-C_3N_4). This material was employed by Reisner and Roy to build a hybrid catalyst with a surface-deposited polymeric cobalt phthalocyanine (CoPPc which monomer being [Co^{II} phthalocyanine] **Co3**, Chart 1) [57]. The resulting system (**Co3@C_3N_4**, Fig. 10) is obtained through *in-situ* polymerization of **Co3** and the two components are linked by π-π stacking interactions that occur between the aromatic centers. In an ACN solution with TEOA under full solar spectrum irradiation (λ > 300 nm) the hybrid generated 1000 μmol g^{-1} of CO after 48 h (TON = 84 based on the Co amount; quantum yield = 0.03% at λ_{ex} = 400 nm) with 85% selectivity (Table 1, entry 5). However, the performance decreases significantly when using only visible light (λ > 400 nm; 607 μmol g^{-1} of CO after 48 h, TON = 51), due to the high UV absorbance of the graphitic semiconductor. Notably, both mechanically mixing CoPPc with mpg-C_3N_4 and polymerizing CoPPC onto non-mesoporous carbon nitride result in hybrid materials that are inactive towards

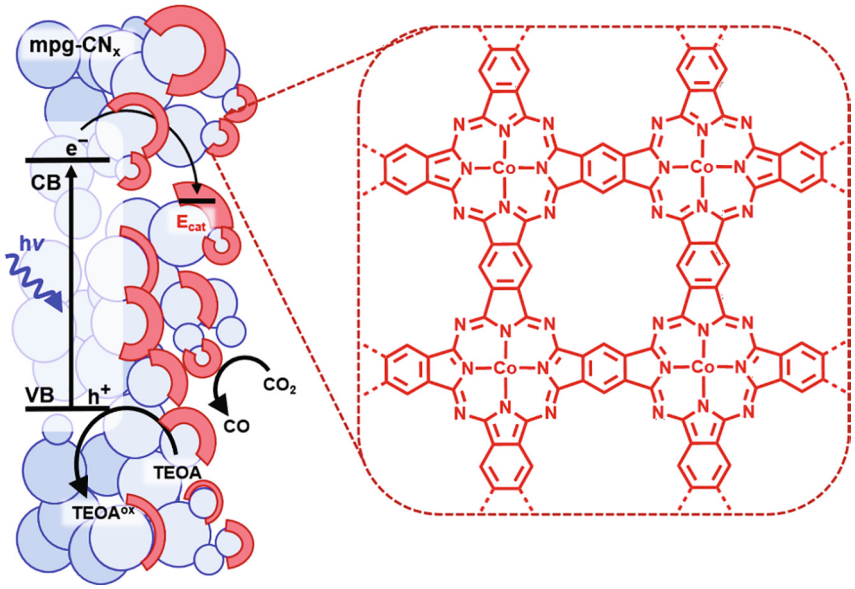

Fig. 10. Illustration of the photocatalytic CO_2 reduction achieved using **Co3@C_3N_4** hybrid system. Adapted from [57].

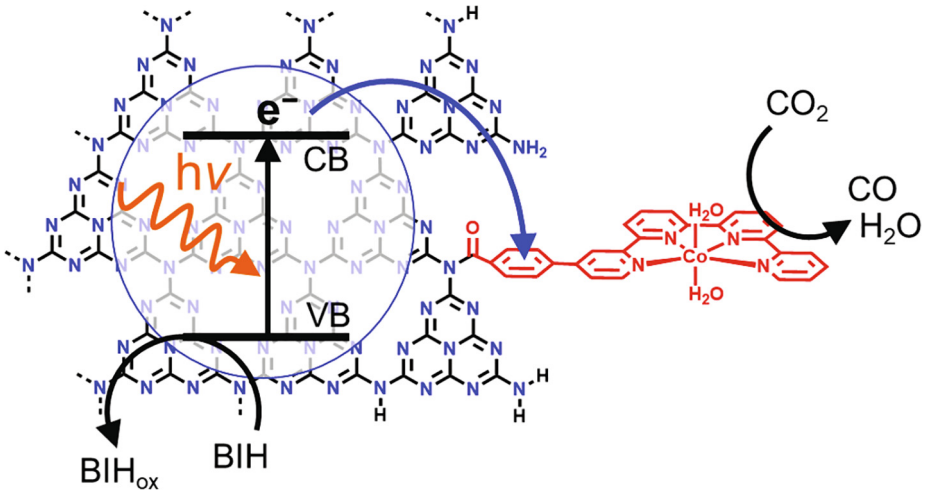

Fig. 11. Illustration of the **Co2@C_3N_4** hybrid system. Adapted from [58].

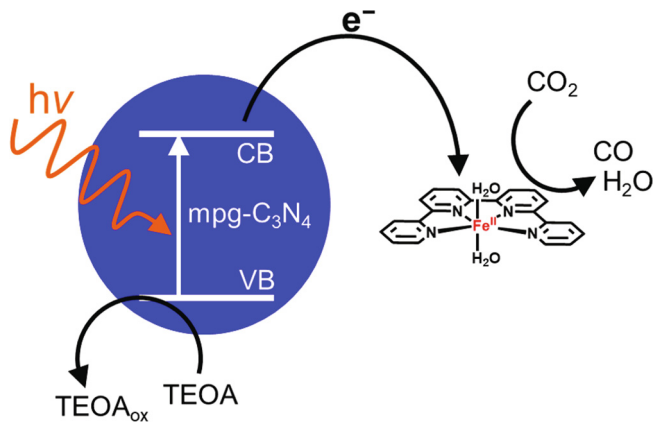

Fig. 12. Illustration of the **Fe1**/mpg-C_3N_4 system. SD = TEOA. Adapted from [59].

CO_2 reduction. This highlights the importance of the *in-situ* polymerization of the catalyst and the mesoporous structure of the support for this system. Spectral changes in the UV–Vis absorption spectra under catalytic conditions are consistent with the reduction of the Co^{II} center to the active Co^{I} species. The reduced Co centers bind to CO_2 then reduced it after a second transfer of a photoexcited electron from the CB of C_3N_4. It must be noted that addition of water to the mixture is deleterious for the catalysis. The reduced activity is likely due to the phase separation of ACN/H_2O/TEOA. Under fully aqueous conditions the TON_{CO} decreased to a value of 5.1.

Recently, Robert, Lau and Ishitani immobilized the **Co2** complex onto mpg-C_3N_4 [58]. The **Co2** was covalent linked by modification of the qpy ligand with a Ph-COOH (Ph = phenyl) moiety in order to form an amide linkage with one of the amine groups of the solid support (Fig. 11). IR spectra of the **Co2@C_3N_4** hybrid show the characteristic peaks of the amide group, confirming the actual covalent grafting. Visible light illumination (λ > 400 nm; 24 h) of an ACN solution containing the hybrid, dimethylphenylbenzimidazoline (BIH) as a SD, and phenol evolved CO with a TON value of 128 and high selectivity (98%, Table 1, entry 6). In contrast, a simple mixture of the complex and the support reaches a TON_{CO} of

only 37 and with a lower selectivity of 88%. This indicates that heterogenization provides a significant performance enhancement. **Co2@C_3N_4** is also highly stable under experimental conditions. To investigate the recyclability of the system, the same catalyst was successfully re-used for four successive 24 h cycles. The results show a remarkable stability of CO production in each cycle highlighting the absence of hybrid degradation during irradiation. In fact, XPS data and UV–Vis absorption spectra confirm that the spectral features of the hybrid are retained after photocatalytic tests. An overall TON_{CO} of 500 was reached after 96 h (apparent quantum yield Φ = 0.25%). This precious-metal-free system represents at the moment the most efficient example of associating mesoporous carbon nitride with a molecular catalyst.

A second system comprising an iron-based complex and mpg-C_3N_4 was reported by Robert and Ishitani [59]. No linkage is present between the two components; In fact, the catalyst is not heterogenized. However, it is worth mentioning this example because it shows the highest selectivity for an Fe molecular catalyst in a colloidal dispersion reported in the literature to date (Fig. 12). The highly active homogeneous **Fe1** catalyst is coupled with mesoporous carbon nitride (which acts as a PS) in an ACN solution containing TEOA as the SD. The mixture is able to produce CO with a TON of 155 and a 97% selectivity (Table 1, entry 7) after 17 h of visible light irradiation (λ > 400 nm). Small amounts of hydrogen and formic acid are also produced. The maximum quantum yield obtained for this system was 4.2% with an excitation wavelength of 400 nm, which is the highest reported so far for systems using carbon nitride for photocatalytic CO_2-to-CO conversion. Complete deactivation of the catalytic system occurred after *ca.* 4 h irradiation *via* the formation of the stable 18-electrons [Fe^0(qpy)(CO)] species. The high selectivity and catalytic activity of this homogeneous system, combined with its instability in contrast to the heterogenized examples discussed, illustrates that heterogenization may significantly alter the catalytic performance. Precise control of the nature of the interactions between a molecular catalyst and its support would allow us to enhance catalytic performance. However, to achieve this a deeper understanding of the relationships between the linkage and catalytic activity need to be established. There is still much work to be done to improve the design of g-C_3N_4 photocatalytic systems.

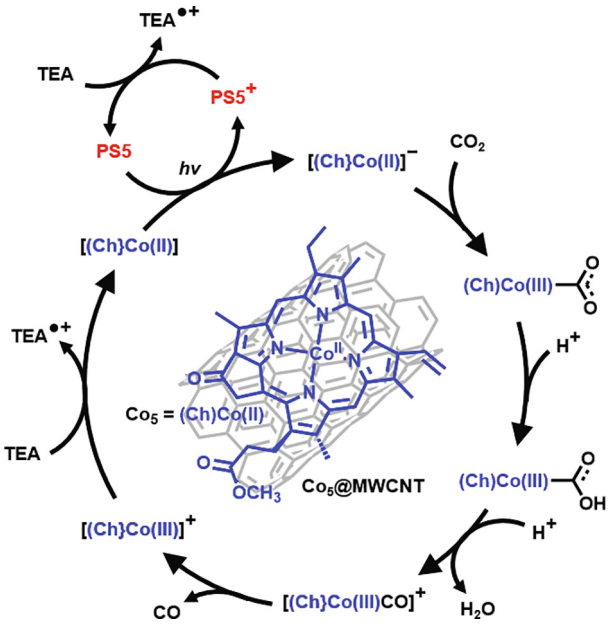

Fig. 13. Proposed mechanism for the hybrid system **Co5@MWCNT** with only the path leading to CO displayed. Adapted from [60].

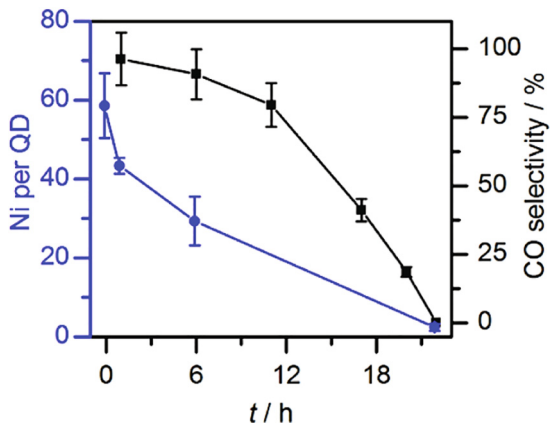

Fig. 14. Changes in product selectivity and catalyst loading over time for **Ni4@CdS**. Reproduced with permission from [61]

3.1.2. Carbon nanotubes

Photocatalytic production of H_2/CO mixtures was achieved employing a [Co^{II}(Ch)] (**Co5**, Chart 1; Ch = Pheophorbide *a* methylester chlorin) complex immobilized onto multi-walled carbon nanotubes (MWCNTs) (to make **Co5@MWCNT**) [60]. In photocatalysis experiments TEOA was used as a SD and [$Ru^{II}(Me_2phen)_3]^{2+}$ (**PS5**, Chart 1; Me_2phen = 4,7-dimethyl-1,10-phenantroline) as photosensitizer. In this case the semiconductive support only acts as a scaffold for **Co5**, while the light is harvested by the homogeneous Ru complex. After 20 h of visible light illumination (λ > 420 nm) in an ACN mixture containing 5% v/v of H_2O, **Co5@MWCNT** was able to evolve CO and H_2 in a 2.4:1 ratio, and with TON values of 501 (Φ_{CO} = 0.10% at λ = 450 nm) and 209, respectively (Table 1, entry 8). The π-π interactions between MWCNTs and **Co5** anchor the complex to the support and may provide a suitable hydrophobic environment for the preferential binding of CO_2 instead of protons. This could explain the selectivity towards CO, as well as the improved performance of the heterogeneous system compared to the MWCNT-free homogeneous system. However, it should be noted that the amount of H_2 produced is greater for **Co5@MWCNT** than homogeneous **Co5**. Likewise, the possible adsorption of the sensitizer at the carbon surface was not investigated, and neither was the possible equilibrium between adsorbed and homogenously dispersed **Co5** complexes. The proposed (classical) mechanism for the reaction is depicted in Fig. 13. Upon photoexcitation, **PS5*** gets reductively quenched by TEA to the monocationic complex, which is able to reduce [Co^{II}(Ch)] to the active [Co^{I}(Ch)]$^-$. The latter species can bind CO_2 ([Co^{III}(Ch)CO_2]$^-$) to form CO, or it can form the hydride [Co^{III}ChH] which leads to H_2.

3.2. Quantum dot supported systems

3.2.1. Cadmium sulfide (CdS)

Aqueous CO_2 reduction is challenging because of the low solubility of the gas in water and the competing H_2 evolution reaction, which is both kinetically and thermodynamically more favorable in an aqueous environment. Despite these limitations, the anchoring of nickel-based catalyst [Ni^{II}(terpyS)$_2$]$^{2+}$ (**Ni4**, Chart 1; terpyS = 2,2′:6′,2″-ter- pyridine-4′-thiol) on light-harvesting CdS quantum dots can afford CO production in a fully aqueous system [61]. CdS is an inexpensive semiconductor with tunable visible light absorption. In addition, CdS QDs have long-lived exited states with

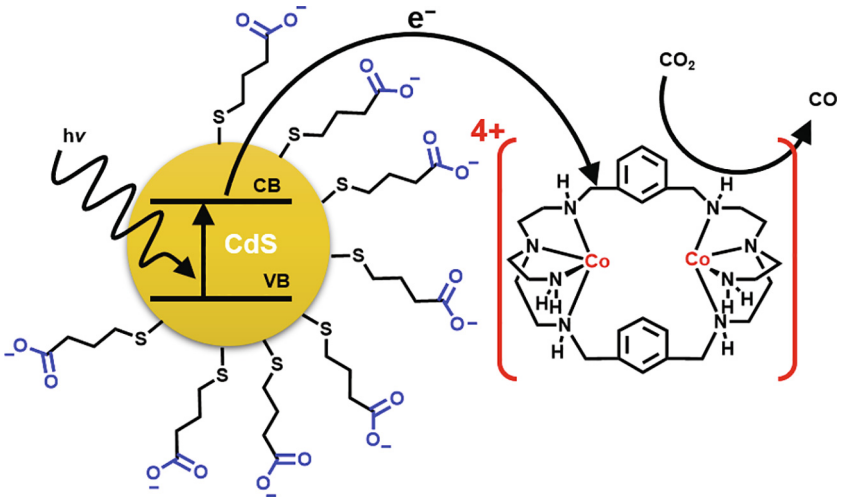

Fig. 15. Illustration of the hybrid system **$Co_2$2@CdS** held together by electrostatic interactions. Adapted from [62].

lifetimes on the same time scale as substrate turnover at the **Ni4** catalyst. Meanwhile, the terpyridine ligand of **Ni4** is easy to functionalize and this has been exploited to try different anchoring groups like phosphonic acid, carboxylic acid, and thiol. The latter was chosen for testing the **Ni4@CdS** system since it allowed the highest catalyst loading on the QD surface.

The photocatalytic activity of the hybrid **Ni4@CdS** was assessed in a H_2O solution containing TEOA as a SD with visible light illumination (λ > 400 nm). The system was able to produce CO with a > 90% selectivity (for the first 8 h) and a TON value of 20 (after 24 h; Φ_{CO} = 0.28% at λ = 400 nm, Table 1, entry 9). After 8 h the selectivity towards CO gradually decreases from 90 to 62 and continues to decrease so that predominantly H_2 is produced after 24 h. The decrease in CO production coincides with the gradual loss of **Ni4** from the QD surface (Fig. 14). Consequently, it was proposed that selective CO production occurs when the photoexcited electrons are transferred to the anchored catalyst. However, as **Ni4** is lost from the QDs more CdS is exposed at the surface and proton reduction can take place at the increasing number of vacant sites. It was also suggested that Ni^{2+} ions released upon catalyst decomposition could also promote proton reduction. However, this study demonstrates the importance of stable anchoring groups in aqueous environments.

A bi-metallic complex, **$Co_2$1** (Chart 1), that had been successfully used for homogeneous CO_2 reduction with the Ru-based photosensitizer **PS4** (Chart 1) was heterogenized and transferred to aqueous media [72]. Zhang and Lu used a modified version of **$Co_2$1** (**$Co_2$2**, Chart 1) with CdS NCs as a photoactive support in a precious-metal-free system for photocatalytic CO_2 reduction [62]. The main difference between **$Co_2$1** and **$Co_2$2** is that the latter lacks a hydrophobic benzene ring in the ligand structure. This makes **$Co_2$2** more water soluble and affords easier access to the active center for CO_2. The negatively charged mercaptopropionic acid (MPA) used to cap the CdS NCs attracted the positively charged **$Co_2$2** complexes and anchored them to the NCs to give the **$Co_2$2@CdS** hybrid (Fig. 15). The hybrid in a $NaHCO_3$ buffer solution containing TEOA as a SD was able to evolve 34.5 μmol of CO (TON = 1380) with 95% selectivity in 120 h under visible light illumination (λ > 420 nm) (Table 1, entry 10). Small amounts of H_2 and CH_4 (0.79 μmol and 1.01 μmol, respectively) were also detected. Using $NaHCO_3$ in this system was found to improve both CO production and selectivity. Notably, similar systems involving CdS nanoparticles bearing neutral ligands, or a positive surface, are 86 and 15 times less active than CdS-MPA in terms of CO production. This highlights the key role played by attractive electrostatic interactions between the two moieties. It is currently thought that the catalytic mechanism for CO_2 reduction at **$Co_2$2** is analogous to the one proposed for **$Co_2$1** because of their similar structures.

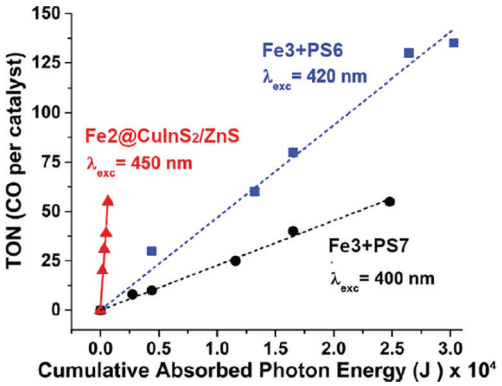

Fig. 16. Measurement of sensitization efficiency and comparison between **Fe2@$CuInS_2$/ZnS** (red), **PS6**- (blue) and **PS7**-sensitized (black) **Fe3** catalyst. Adapted with permission from [63].

3.2.2. Copper indium sulfide/zinc sulfide ($CuInS_2$/ZnS)

The **Fe2** porphyrin catalyst was noncovalently bound to the photoactive support $CuInS_2$/ZnS core/shell QD to make a photocatalytic system for CO_2 reduction [63]. The QD surface is capped with 3-mercapto-1-propanol, which makes it soluble in DMSO and in addition the sulfur-enriched surface allows the noncovalent interaction of the QD with **Fe2** through the iron centers ("face-on" adsorption geometry). Moreover, the reduction potential for this QD (around −2.4 V *vs.* SCE) is negative enough to perform all three Fe-centered reductions required to obtain the Fe^0 active species of **Fe2**. Catalytic tests performed in DMSO with the hybrid **Fe2@$CuInS_2$/ZnS** and N,N,N′,N′-tetramethyl-*p*-phenylenediamine (TMPD) as the SD could produce CO with a TON of 55 (450 nm monochromatic irradiation for 40 h; Φ = 0.01%) and 84% selectivity (the rest being H_2) (Table 1, entry 11). One way to measure sensitization efficiency (defined as the number of CO molecules produced per joule of absorbed photon energy per catalyst molecule) is to plot the TON_{CO} *vs.* the cumulative photon energy absorbed (J) by the sensitizer (a parameter that is proportional to light intensity, illumination area, time and fraction of absorbed photons). The sensitization efficiency of **Fe2@$CuInS_2$/ZnS** during

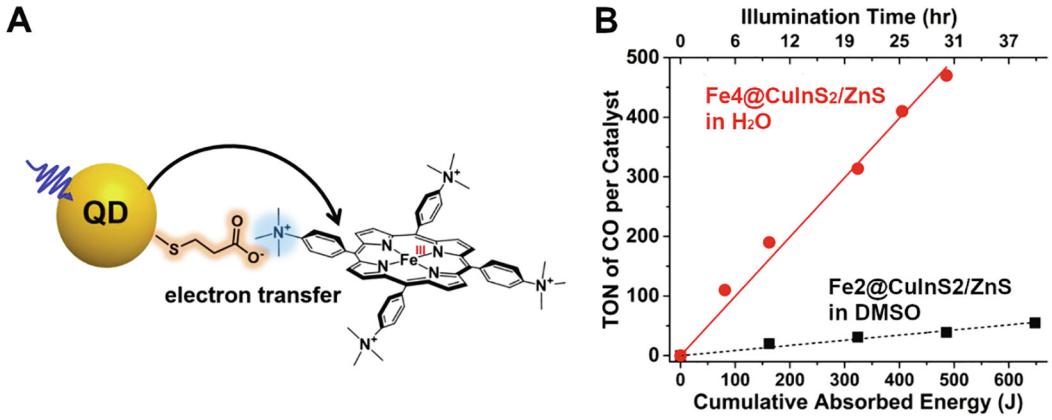

Fig. 17. a. Schematic representation of electron transfer and electrostatic interactions in the **Fe4@CuInS$_2$/ZnS** hybrid system; **b.** comparison of sensitization efficiency between the **Fe4**- (red) and **Fe2**-containing (black) systems. Adapted with permission from [64].

photocatalysis was compared with those of two homogeneous systems, **Fe3** sensitized by **PS6** and **Fe3** sensitized with **PS7** (Chart 1 and Fig. 16). As can be clearly seen by Fig. 16, the QD-sensitized system has a tremendous sensitization efficiency compared to the **PS6**-sensitized (18 times more efficient) and the **PS7**-sensitized (36 times more efficient) systems. Electron transfer in the two **Fe3** systems relies on collisions between freely diffusing sensitizers and catalysts, which is regulated by bimolecular reaction kinetics. On the other hand, a significant electronic coupling exists between **Fe2** and CuInS$_2$/ZnS which is established through noncovalent interactions, and this could enable the ultrafast electron transfer between the two components (reduction of the Fe^{III} species to Fe^{I} takes < 200 fs), which is in turn the origin of the high sensitization efficiency of the hybrid.

The same group designed a second, similar hybrid system for aqueous conditions employing the same QD coupled with the **Fe4** (Chart 1) catalyst [64]. Here, the capping ligands on the surface of CuInS$_2$/ZnS nanoparticles are MPA molecules, with the carboxylate end pointing outwards. Contrary to the binding mode in the **Fe2@CuInS$_2$/ZnS** system, the **Fe4@CuInS$_2$/ZnS** hybrid is attached by electrostatic interactions that exist between the negatively charged carboxylate ends of the QDs and the positive charges borne by the trimethylammonium groups of **Fe4** (Fig. 17a). This was supported by UV–Vis spectroscopy measurements. The catalytic activity of this system can be enhanced by adjusting the electrostatic interactions between the components with a controlled addition of K$^+$ ions; adjusting the ionic strength of the aqueous solution controlled the size of the **Fe2@CuInS$_2$/ZnS** assemblies. The TON increased from 51 (no K$^+$ added) to 124 (5 mM of K$^+$ added; values measured after 5 h of illumination) as the size of the supramolecular assemblies decreased from 35 to 19 nm. The dependence of assembly size and catalytic activity on K$^+$ concentration was explained in terms of electrostatic repulsion. Some of the carboxylates become protonated in the CO_2-saturated mixture which allows the QDs to aggregate through decreased repulsion and increased hydrogen bonding, rather than coordinating to the catalyst. Such aggregation prevents efficient sensitization of the iron catalyst and results in a lower CO_2 reduction activity. However, the presence of positive charged potassium ions reduces the apparent pKa of the carboxylates and therefore induces their deprotonation and consequent disaggregation of the QD assemblies. At this point **Fe4** can sufficiently interact with the colloid photosensitizer and carry out efficient catalysis. The optimized aqueous **Fe4@CuInS$_2$/ZnS** system under extended illumination (30 h, λ = 450 nm) with TEOA as the SD, was able to yield CO with a TON of 450 (Φ = 0.025% at 420 nm), TOF of 16 h^{-1} and 99% selectivity (Table 1, entry 12). Compared to the **Fe2@CuInS$_2$/ZnS** hybrid analyzed earlier, the present system has a sensitization efficiency 11 times higher, as can be seen in Fig. 17B. CO_2 is 10 times less soluble in H_2O than in DMSO, which was the solvent employed with the **Fe2**, but the aqueous system is still more efficient. The enhanced photocatalytic activity of the aqueous system can be explained by the attractive electrostatic interactions between the catalyst and sensitizer. Dynamic light scattering (DLS) measurements of the particle size showed that **Fe4** and CuInS$_2$/ZnS are able to form superstructures which are larger than a single QD-CAT assembly and are comprised of several units of each component. **Fe4** has four positively charged groups that can bind four separate negatively charged QDs, which is likely to happen with the 1:30 stoichiometry used in the experiment. Such a structure, with multiple sensitizers electronically coupled to one catalyst, should ensure a very efficient funneling of photoexcited electrons to the latter, which significantly enhances the sensitization efficiency of the system as shown in Fig. 17B.

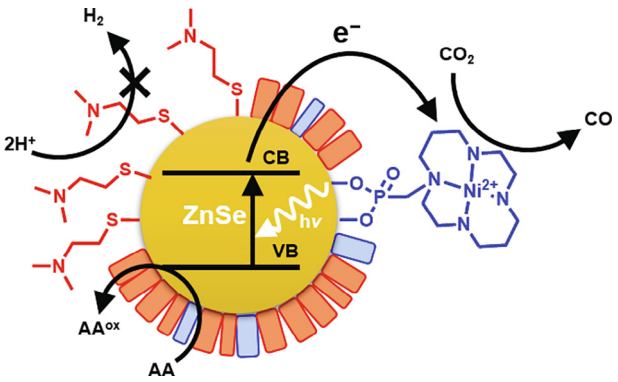

Fig. 18. Schematic representation of the hybrid system **Ni2@ZnSe** with the QD particle partially capped by MEDA. AA: ascorbic acid. Adapted from [65].

3.2.3. Zinc selenide (ZnSe)

In line with the ongoing efforts to replace toxic and expensive photosensitizers with cheap and benign materials, Reisner *et al.* developed a Cd-free hybrid system based on ZnSe quantum dots [65]. The catalyst chosen for the system is a modification of the **Ni1** cyclam complex, to which a phosphonic acid anchoring group has been added to form the [Ni^{II}(cyclamP)] (**Ni2**, Chart 1) complex. ZnSe is a stable semiconductor with a bandgap of 2.7 eV and CB located around −1.4 V *vs.* NHE which is negative enough to trigger CO_2 reduction with **Ni2** (onset reduction potential: −1.0 V *vs.*

NHE). The photocatalytic performance of the **Ni2@ZnSe** hybrid with uncapped QD particles has been studied under visible-light irradiation (λ > 400 nm) for 20 h with ascorbic acid as the SD. The system was able to produce CO with a Ni-based TON of 121, albeit with the low selectivity of 8%. H_2 is the major product and consumes most of the photoexcited electrons supplied by the QD. H_2 generation is still active after 20 h of illumination while the CO yield decreases. This is probably due to deactivation of the nickel catalyst. Comparative tests conducted with the analogue **Ni1** in homogeneous conditions showed that the **Ni2@ZnSe** hybrid is much more efficient than the one with the freely diffusing catalyst, indicating that catalyst immobilization improved CO_2 reduction.

The performance of the hybrid **Ni2@ZnSe** was further enhanced by controlled QD ligand capping (Fig. 18) [65]. When 2-(dimethylamino)ethanethiol (MEDA) was added to the mixture, part of the QDs surface was passivated by this molecule. Since H_2 evolution occurs on the nanoparticle surface, it was partially suppressed in the MEDA-capped system. Using an optimized amount of MEDA (25 μM), it was possible to increase the selectivity toward CO production from 8.0% to 33.8%. Furthermore, capping the QD with MEDA also increased CO production, rising the TON_{CO} to 283 after 20 h (Table 1, entry 13), presumably because more photoexcited electrons are available for the anchored molecular catalyst. A high quantum yield of 3.4% was recorded for illumination of the MEDA-modified hybrid with 400 nm monochromatic light for 6 h.

3.3. Metal oxide scaffolds

3.3.1. Titanium oxide (TiO_2)

Beside quantum dots, ligand functionalized variations of **Ni1** cyclam catalyst have also been immobilized on different metal oxides supports. When this catalyst is modified with an anchoring carboxylic acid group, [Ni^{II}(cyclamC)] (**Ni3,** Chart 1), it can be grafted onto nanocrystalline TiO_2 with a monodentate binding mode through the C=O moiety [73]. Photocatalytic CO_2 reduction tests could not be performed with the resulting hybrid **Ni3@TiO$_2$** because the system is not stable enough in a CO_2-containing ACN mixture. Nonetheless, this setup has been useful to assess the factors controlling charge transfer to the anchored molecular catalyst. Transient absorption spectroscopy (TAS) is an effective tool to study the dynamics of photoexcited electrons and holes in semiconductors like titanium oxide. When exciting pure TiO_2 with λ = 355 nm and employing TEOA as hole scavenger, the sample shows long-lived photoelectrons with a half-life time ($t_{50\%}$) of 0.8 s thanks to the suppression of the electron-hole recombination process exerted by TEOA. In contrast, experiments with **Ni3@TiO$_2$** in identical conditions present a photoelectron decay rate that is over two orders of magnitude faster ($t_{50\%}$ = 1.2 ms) than the control test with pure TiO_2. The short life of photoelectrons in this case (even in presence of the SD) is indicative of an efficient electron transfer from the semiconductor to the immobilized catalyst. Moreover, data obtained using non-functionalized homogeneous catalyst **Ni1** reveal that the transfer of electrons to the complex is an order of magnitude slower ($t_{50\%}$ = 20 ms) than that observed with the heterogenized **Ni3**. This highlights the positive role that surface anchoring has on electron transfer kinetics. There are two key parameters that control the rate of photoelectron funneling towards the adsorbed catalytic center: the distance between the semiconductor and the active metal, and the thermodynamic driving force for electron transfer. The latter was assessed by anchoring **Ni3** to a second active support, a mixed $Ti_{1-x}ZrxO_2$ (x = 0.2) semiconductor, which has an increased driving force (ΔG = −0.65 eV) compared to **Ni3@TiO$_2$** (ΔG = −0.5 eV). Accordingly, TAS measurements on **Ni3@Ti$_{1-x}$Zr$_x$O$_2$** show a marked increase in the rate of photoelectron decay ($t_{50\%}$ = 800 μs) compared to **Ni3@TiO$_2$**, indicating that optimization of the driving force for electron transfer to the catalyst is important for efficient charge transfer.

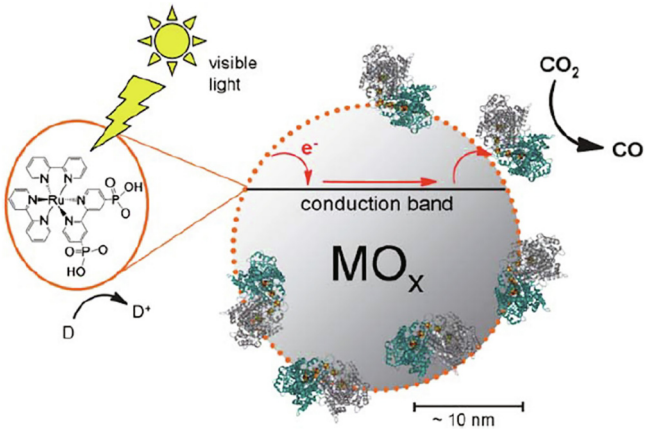

Fig. 19. Illustration of CO_2 reduction at the CODH- and **PS1**-modified TiO_2 surface driven by visible light. D: MES. Adapted from [68].

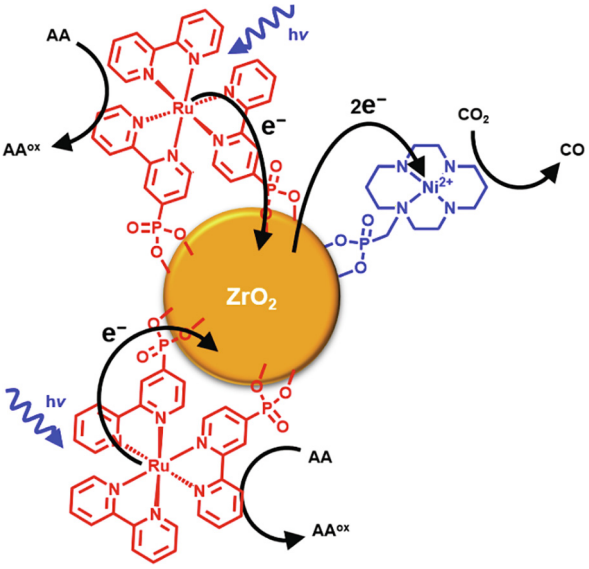

Fig. 20. Nickel catalyst and ruthenium photosensitizers co-immobilized on a ZrO_2 particle to form **Ni5@ZrO$_2$** hybrid system. Adapted from [69].

As a low cost and non-toxic material, titanium oxide is used widely in the solar energy conversion field. It suffers from one major drawback, however, lack of absorption in the visible light range. Nonetheless, it has been employed in many studies. One example is the work published in 2014 by Li *et al.* in which they deposited cobalt catalyst **Co1** onto commercially available TiO_2 nanoparticles (Degussa, P25) [66]. FTIR and XPS spectra show that Co-O bonds were present in the resulting hybrid **Co1@TiO$_2$**, thus indicating that the molecular complex was linked to the hydroxyl groups present on the surface of the P25 nanoparticles. The hybrid could produce CO and H_2 as major products (Table 1, entry 14) with a ratio around 1:1 and a TON_{CO} = 20 after 4 h of UV light irradiation (Hg lamp; TEOA as SD; aqueous environment). Both **Co1** and the titania surface contributed to the H_2 production, but only the molecular catalyst is active towards CO_2-to-CO reduction. Diffuse reflectance infrared Fourier transform spectroscopy (DRIFTS) indicated that CO_2 reduction at the heterogenized **Co1** might proceed *via* a formate-bridged dimer. When the homogeneous **PS1**

was added to the mixture containing the hybrid, CO was evolved with a TON value of 35 under visible light irradiation (λ > 420 nm). However, the selectivity for CO_2 reduction decreased dramatically to give a CO:H_2 ratio of 0.2.

In a separate study, a Mn complex (**Mn1,** Chart 1) was covalently attached to a TiO_2 support sensitized with the organic dye **PS8** (Chart 1) [67]. Phosphonic acid anchoring groups were attached to the Mn-center via a bpy linker group, while **PS8** was co-anchored to the TiO_2 through a carboxylic acid moiety. Under illumination (λ > 400 nm) for 26 h in a DMF suspension with BIH as a sacrificial electron donor, the **Mn1/PS8@TiO$_2$** hybrid produced formate with enhanced selectivity at low catalyst loadings (TON_{HCOO-} 60, TON_{CO} < 1, see Table 1, entry 15). However, as the catalyst loading was increased the selectivity and TON decreased. The authors proposed that at higher loadings **Mn1** formed dimers on the support that participate in a second pathway that produces CO. Despite problems with light scattering off the colloidal particles, the heterogenized **Mn1** exhibited improved catalytic performance for formate production compared to the homogenous analogue with **PS1** which was only stable for 8 h (TON_{HCOO} 8.6, TON_{CO} 52.6).

An interesting comparison can be made between the metal oxide supported molecular catalysts and a system comprising an immobilized enzyme, carbon monoxide dehydrogenase (CODH), on TiO_2 sensitized with a phosphonic acid-modified Ru-sensitizer **PS3** ([Ru^{II}(2,2′-bipyridine)$_2$(2,2′-bipyridine-4,4′-diylbis(phosphonic acid))], Chart 1 and Fig. 19) [68]. The CODH@TiO_2 hybrid was able to photocatalyze CO_2-to-CO reduction with a TON of around 2000 and 100% selectivity after 4 h of visible light irradiation in an aqueous of the SD, 2-(N-morpholino)ethanesulfonic acid (MES) (TOF_{CO} = 504 h^{-1}; λ > 420 nm; pH 6; 20 °C; Φ_{CO} = 0.07%). The high TON and selectivity (Table 1, entry 16), as well as mild aqueous operating conditions, make immobilized enzymes an appealing alternative to molecular catalysts. However, they are currently extremely fragile, as well as expensive and difficult to purify [65].

3.3.2. Zirconium oxide (ZrO_2)

In addition to TiO_2 and mixed titanium- zirconium oxide, **Ni2** has also been anchored onto ZrO_2 particles sensitized with **PS3**

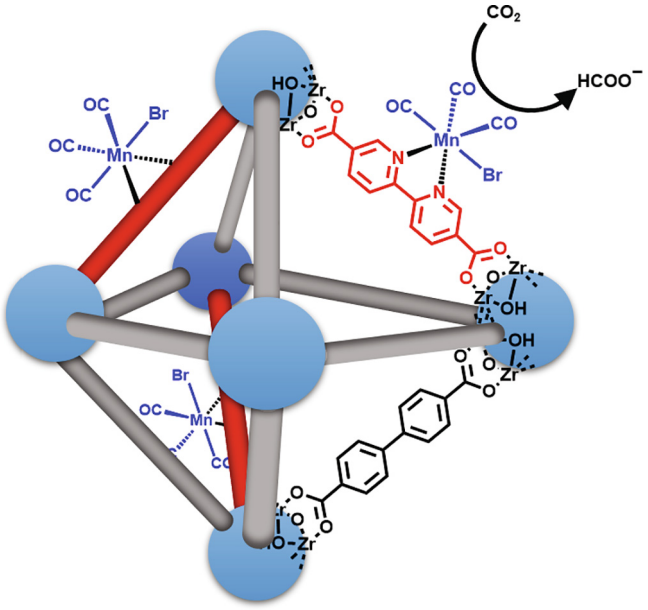

Fig. 21. Representation of the **Mn1@UiO-67** hybrid structure catalysing CO_2 reduction after electron transfer from **PS2**. The bipyridine modified bridging ligands (red) are shown coordinated to the catalyst (**Mn2** blue) and octahedral zirconium oxide corner units (light blue). Adapted from [70].

to produce the **Ni2@ZrO$_2$** hybrid system (Fig. 20) [69]. Unlike the **Ni3** complex, **Ni2** has a phosphonic acid anchor which allows it to bind more firmly to the metal oxide surface and remains stable even in acid aqueous environments (pH 4). This meant that photocatalytic experiments could be performed with **Ni2@ZrO$_2$**, unlike **Ni3@TiO$_2$**. The hybrid was tested in an ascorbate buffer (SD, pH 4) mixture under UV–Vis illumination (λ = 375–795 nm) and after 7 h it produced CO and H_2, with a marked preference for the latter (H_2:CO ratio of 4.15:1, Table 1, entry 17). CO was obtained with the relatively high rate of 322 μmol h^{-1} g^{-1} and a TON value of 4.8, which is low but an improvement on the efficiency of the fully homogeneous system employing **Ni1** and **PS1** (TON_{CO} = 0.1).

Being an inert support, ZrO_2 requires sensitization to carry out the catalysis. As the light-driven reduction of CO_2 to CO is a multi-step process requiring the delivery of two electrons to **Ni2** per catalytic cycle, it follows that multiple light absorbers per catalytic center would be advantageous. This idea was tested by anchoring **PS3** and **Ni2** to **ZrO$_2$** in different ratios [69]. It was found that 2.6:1 **PS3**:**Ni2** was the optimum ratio. As expected, increasing the dye-loading with respect to the catalyst appeared to improve electron transfer from the photoexcited sensitizer to the molecular catalyst and result in enhanced photocatalytic efficiency.

3.4. Perovskites

Very recently, a study reported the non-covalent immobilization of **Ni5** on inorganic ligand-capped $CsPbBr_3$ perovskite NCs [32]. The resulting hybrid had an absorption range up to 600 nm, thus showing that the $CsPbBr_3$ moiety played the role of the PS, and **Ni5** the role of catalyst since the latter alone does not absorb in the visible range. When 5 mg of the hybrid was dispersed in 5 mL of a 49:1 (v:v) ethyl acetate:water mixture, under 100 mW cm^{-2} visible (>400 nm) light irradiation, CO_2 was converted into CO (*ca.* 1500 μmol g^{-1}) and CH_4 (*ca.* 225 μmol g^{-1}) with a total yield of 1724 μmol g^{-1} after 4 h with an optimized **Ni5** loading (Table 1, entry 18). Isotope ^{13}C-labelled experiments confirmed that products indeed originated from CO_2. This hybrid outperformed the performance observed with the perovskite NCs alone by a 26-fold factor. This study illustrates the possibility of utilizing halide perovskite NCs as new platforms for photocatalytic applications.

3.5. Metal-organic frameworks (MOFs) and covalent organic frameworks (COFs)

As mentioned in Section 2.4, metal–organic frameworks (MOFs) are extended ordered molecular networks assembled from bridging organic ligands connecting metal ions. They have emerged as an intriguing class of crystalline and microporous materials with a vast array of applications ranging from gas absorption, molecular separation and drug delivery, to catalysis and chemical sensing. Specifically, the ability to design and tune the functional components of the organic linkers present in the material, along with inherently high porosity, allows MOFs to be a versatile platform for artificial photosynthesis [70].

3.5.1. UiO-67

The MOF UiO-67-bpydc is Zr^{IV}-based with dicarboxylate bridging ligands and open bipyridine chelating groups. The metal complex $Mn(CO)_5Br$ was incorporated into the UiO-67-bpydc framework to make the hybrid catalyst **Mn2@UiO-67** (Fig. 21). Here the MOF not only acted as a support material and molecular cage for the catalyst [Mn^{I}bpy$(CO)_3$Br] (**Mn2**, Chart 1), but also as a ligand; the Mn-center coordinates to unoccupied coordination sites on the MOF ligands located inside the pores of the MOF [70]. Notably, this mode of anchoring the catalyst is different to

most of the other examples we have discussed, as the linker and anchoring group are part of the support and are pre-assembled in an ordered structure. Visible light irradiation (λ = 470 nm) of a DMF/TEOA solution containing **Mn2@UiO-67**, homogeneous **PS2,** and benzyl-dihydronicotinamide (BNAH) as the SD, afforded formate with a high selectivity (96%) and a TON of 110 after 18 h (Φ_{CO} = 6.74%, Table 1, entry 19), together with small amounts of CO and H_2. **Mn2@UiO-67** out-performed both a fully homogeneous **Mn2**/**PS2** solution and a mixture of homogeneous **Mn2** and UiO-67 in formate production. This clearly demonstrates that the incorporation of the manganese catalyst in the MOF structure enhances the catalysis. This enhancement is thought to be partly due to stabilization of the labile carbonyl ligands of the $Mn(CO)_3$ catalyst, and inhibition of dimerization of the catalyst which was a problem for **Mn1/PS8@TiO$_2$** [67]. The proposed catalytic mechanism begins with the reduction of the Mn^I moiety to the radical species (Mn^0) by the reductively quenched **PS2**. Then, a Mn^I-H hydride is formed through the donation of an H^+ and an e^- from TEOA. Subsequently, CO_2 insertion into the metal- hydride bond affords the formate moiety, which dissociates to restore the initial Mn^I species. Recyclability studies showed significant formate production even after three consecutive 4 h photocatalytic runs. The hybrid retained ~48%, ~38%, and ~34% activity after one, two and three 4 h experiments, respectively [70]. Post-catalysis characterization suggests that the decrease in photochemical performance is likely due to loss of the $Mn(CO)_3$ moiety from the framework as a result of prolonged irradiation and exposure to the reaction solution.

MOFs with Fe-O clusters as corner units have been reported as CO_2 reduction photocatalysts without the need for modification with catalysts or **PS**s [74]. Exposed Fe centers at vacant coordination sites on the clusters act as active sites for the reduction of CO_2 to formate. Photo-excitation occurs at both the clusters and bridging aromatic ligands with uncoordinated amine groups. The presence of these amine groups activates photo-excitation of the ligand and increases CO_2 uptake. For instance, MIL-101(Fe) generated 1.18 mmol of formate per g of MOF after 8 h of illumination and NH_2-MIL-101(Fe) generated 3.56 mmol of formate per g of MOF under the same conditions (λ > 420 nm 8 h ACN, TEOA 5:1). Catalytically inactive Ui-O66(Zr) has been activated for photocatalytic CO_2 reduction by incorporating similar amine functionalized ligands to produce 0.264–0.414 mmol formate per g of MOF after 10 h illumination in ACN, TEOA (5:1) [75]. Although these heterogeneous photocatalysts are not strictly speaking based on molecular complexes, they highlight unusual MOF-specific behavior as well as the importance of ligand effects when making heterogeneous catalysts in this way.

In another interesting study, a Zr MOF (PCN-222) was made with bridging ligands incorporating vacant porphyrins and doped with increasing amounts of Zn ions [76]. Doping PCN-222 increased the photocatalytic activity of the system towards CO_2 reduction. This example is particularly interesting because the best catalytic activity was obtained when only 5% of the porphyrin sites were filled; during 4 h of visible light illumination (in H_2O/ethylene glycol, 20:1) 5% PCN-222(Zn), 25% PCN-222(Zn), and PCN-222 generated formate at 345, 158, 28.7 mmol/g/h, respectively. A similar MOF with porphyrin bridging ligands was used to make a hybrid photocatalytic material for CO_2 reduction to CH_4 and CO [31]; PCN-221 was used to encapsulate perovskite QDs and doped with Fe cations to activate the porphyrins for catalytic production of methane. The MOF structure held the catalytic sites in close proximity to the QD PS to enhanced electron transfer, as well as stabilizing the QD for up to 80 h illumination [31]. The highest selectivity for CH_4 (66%) was obtained with the hybrid $MAPbI_3$@-PCN-221($Fe_{0.2}$) which generated at total of 1.59 mmol CO_2 reduction products per gram of MOF (CH_4 and CO) over 80 h of illumination in an ethylacetate water mixture (Table 1, entry 20). Without the QD, the same material gave a total yield of 0.41 mmol per gram of MOF. For this system, higher proportions of Fe ions decreased the selectivity for CH_4 production. Encapsulating support material inside MOFs, as shown here, could potentially be used to heterogenize molecular catalysts onto supports with chemistry that is less amenable to the other anchoring methods presented in this review.

3.5.2. Zif-9

Zeolitic imidazolate frameworks (ZIFs) are a subclass of MOFs possessing high chemical and thermal stabilities, and they exhibit great potential for CO_2 capture. The cobalt-containing benzimidazolate MOF (**Co-ZIF-9**) is itself a "hybrid" catalyst very different from the ones described until now [47]; the benzimidazolate ligands and the Co^{II} center make up the entire microporous MOF structure and the Co-centers connect the MOF ligands to each other, rather than sitting in the pores as demonstrated by the **Mn1@UiO-67** system, or connecting the ligands with metal oxide clusters. Hence, there is no added support material for this heterogenized catalyst (Fig. 22).

CO_2 reduction reactions were conducted using **Co-ZIF-9** under visible-light illumination (λ > 420 nm) with **PS1**, and TEOA as the SD. Upon irradiation CO and H_2 were produced for 30 min at a reaction rate of 1.4 μmol min^{-1} and 1.0 μmol min^{-1}, respectively. Comparative tests revealed that the homogeneous system of benzimidazolate and Co^{2+} (together with PS1) was able to photo-

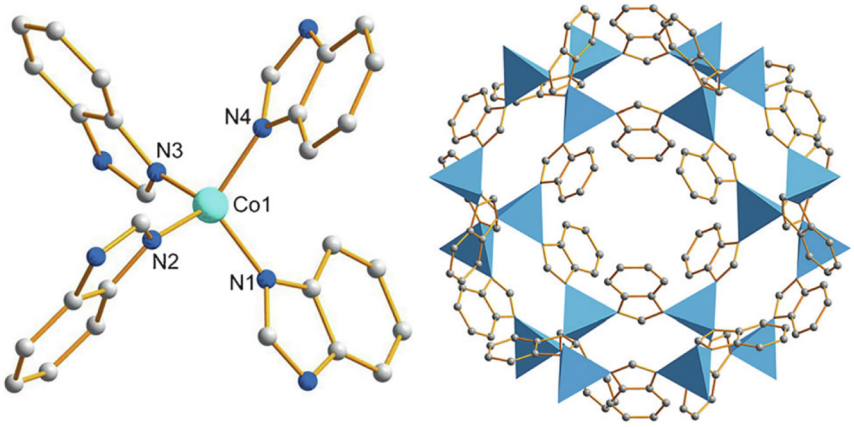

Fig. 22. Chemical structure of **Co-ZIF-9**. Ball and stick representation showing the coordination environment around the cobalt (left); packing diagram of **Co-ZIF-9** (right). Co: light blue; C: gray; N: blue. Reproduced with permission from [47].

catalyze the production of CO and H_2 but at lower rates. This demonstrates that the **Co-ZIF-9** structure and not just the components plays an important role in the catalytic reduction. During the initial 30 min of the reaction the total amount of CO and H_2 increased drastically, however, afterwards it only increased slightly. This decrease in catalyst turnover is attributed to photobleaching of the PS rather than catalyst decomposition or deactivation. To check the stability of the catalyst, used **Co-ZIF-9** was recovered from the reaction mixture and then re-dispersed in a fresh PS solution for 30 min five consecutive times. The activity of the reused catalyst presents no noticeable alteration and the cumulative TON value for CO and H_2 is 450 after 2.5 h (Table 1, entry 21). This result highlights the high stability of the MOF in the photocatalytic system.

3.5.3. COFs

From the examples that we have discussed it is evident that MOFs offer many advantages in heterogeneous photocatalysis. Specifically, changing the constituent ligands and metallic groups can be used to control CO_2 adsorption and catalyst-PS separation. However, the coordination bonds that hold MOFs together are weaker than covalent bonds and, as a result, covalent organic frameworks (COFs) have been developed as an alternative to MOFs [71]. COFs are crystalline π-conjugated polymers with controllable pore sizes, and they can be synthesized with the electronic properties of semi-conductors. In fact, g-C_3N_4 can fall into the COF category. Molecular complexes can be incorporated into COF architecture. For example, a Co-porphyrin (**Co6**) was connected with phenyl linkers, similar to those used in MOF chemistry, to make different COFs containing cobalt and copper porphyrins [77]. These 2D materials were used as electrocatalysts in CO_2 reduction and could reach TON_{CO} values of up to 9400 per electroactive porphyrin. The electrocatalysts had an overpotential of −0.55 V in an aqueous pH 7 buffer and mixed metal species were investigated [77]. The **Co6** COF was similar to polymerised **Co3** used to make the **Co3@C_3N_4** hybrid [57], however, the COFs have more controllable pore sizes. The **Co7@C_3N_4** example also employed COF-like chemistry [54]. It is worth noting that in non-metallic/water-splitting examples COF ligands have also been modified to decrease their bandgap to the visible range. However, this does not appear to have been applied to the field of CO_2 reduction photocatalysis yet.

Although COFs exhibit properties that make them excellent candidates as support materials, COF research in CO_2 photocatalysis has mainly been directed at enhancing their inherent photocatalytic properties to make metal-free heterogeneous photocatalysts [71,78]. COFs have been combined with precious metal molecular catalysts for photocatalytic CO_2 reduction [79]. In one example, however, 2, 6-diaminoanthracene (DATP) and 2, 6-diaminoanthraquinone (DQTP) were used to connect phenyl units in two different COFs which were then metallated with salts of Zn, Ni and Co [71]. The anthraquinone groups acted as ligands, and strongly coordinated the metal centers to construct molecular catalysts within the pores of the DQTP COF. **Co DQTP COF** was the most active material and produced 0.815 mmol CO over 4 h illumination (1.02 mmol $g^{-1}h^{-1}$) dispersed in a solution of **PS1** and ACN/TEOA 4:1 (Table 1, entry 22). This corresponds to a TON of 2.18, presumably per metal site. The selectivity for this reaction was 59.4% for CO over H_2. Changing the solvent or sacrificial electron donor in this system altered to the reaction to produce formic acid instead of CO [71]. Using the same conditions and catalyst but changing the solvent to N,N-dimethylacetamide produced 0.947 mmol of formic acid (Table 1, entry 23). Ni DQTP COF and Zn DQTP COF exhibited improved performance for the production of formic acid compared to CO. In fact, Zn DQTP COF produced formic acid with the highest selectivity of the COFs at 90% (TON 0.33). Although the TON values for these materials are lower than some examples that have been presented, they are some of the first examples of COFs for photocatalytic CO_2 reduction that incorporate group 4 and first row transition metal molecular catalysts. The high selectivity exhibited and the tunability of these materials in combination with the high TON reported for the electrocatalyst example, show that heterogenization of CO_2 reduction catalysts within COFs is an important, growing field [71,77]. Recent advances in COF pore functionalization offer new opportunities for more flexible post-synthetic derivatization of COFs with catalysts. For example, Lotsch and co-workers recently used click chemistry to immobilize different cobaloxime water splitting catalyst into COF pores [49]. The same group also recently developed a novel strategy for constructing COFs with amine sites within the pore architecture which could be modified using protection and deprotection strategies [50]. This is an exciting development that could be crucial to future work in this field.

3.6. Photoelectrochemical (PEC) conversion

In the examples discussed so far PSs have either been dissolved in solutions used to disperse heterogenized catalysts, the support material itself was the PS, or the PS was anchored to the support material alongside the catalysts. Electrocatalysis and photocatalysis can be combined in a photoelectrochemical (PEC) approach to achieve light-driven CO_2 reduction by immobilizing molecular catalysts onto photoelectrodes [6]. In CO_2 photoelectrochemical reduction, dye-sensitized photocathodes (DSPC) are often employed as the photoelectrodes. DSPCs are usually made by modifying wide bandgap *p*-type semiconductors with light-harvesting compounds and this architecture allows catalysts to be attached using the same kind of chemistry discussed in this review for metal oxide and chalcogenide systems. The co-anchored catalysts can then be photo-reduced in the same manner. When paired with a photoanode in a PEC tandem device (PEC cell), the electrons for the regeneration of the photosensitizer can be supplied directly from the oxidation half-reaction occurring at the photoanode instead of commonly used SDs. A SD is still required for the reaction at the photoanode/anode, however, this can be water, or an economically useful reactant. Separation of the oxidation and reduction products at different photo/electrodes is also advantageous for product purification and safety. Examples of dye-sensitized photocathodes for molecular-based water oxidation currently far outnumber those of their DSPC counterparts for CO_2-to-fuel conversion. Moreover, when only precious metal-free systems are considered, literature offers just a handful of examples. However, if the electrolytes are similar and the photoelectrode absorption profiles do not overlap significantly, DSPCs can theoretically be employed with photoanodes developed for water splitting cells with minimal optimization.

In a PEC cell setup with water as the reductant (SD), the oxygen evolution reaction has been considered a major obstacle for solar fuel generation due to the multiple PCET steps. Moreover, simultaneously achieving CO production and H_2O oxidation remains a great challenge because of the competition between CO_2 conversion and H^+ reduction that is always present in aqueous solutions [80].

A very recent study features a photoelectrochemical cell composed of a $BiVO_4$ photoanode modified with a fluorinated cobalt complex (cubane derivative) and a carbon cloth cathode modified with the perfluorinated functionalized phthalocyanine (**Co4**, Chart 1 and Fig. 23) [80]. The light only drives the water oxidation half-reaction, which generates electrons and protons that subsequently migrate into the cathodic compartment of the cell, where the cathode functions just like a classic electrode and **Co4** as an electrocatalyst. Photocathodes often demonstrate limited activity

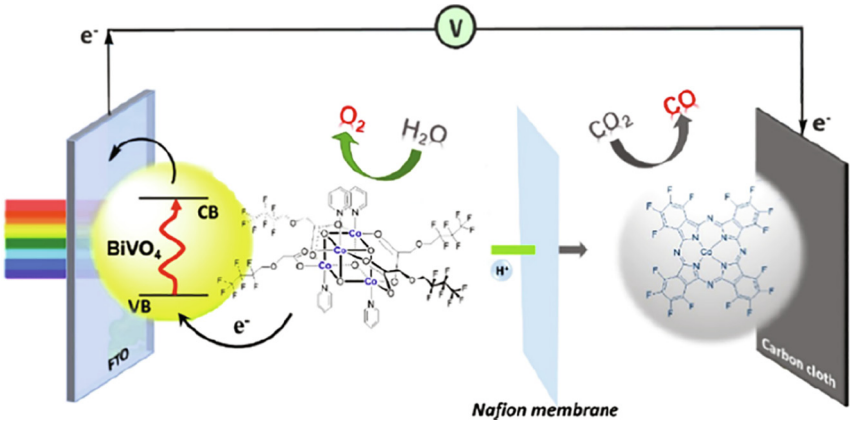

Fig. 23. Schematic illustration of the PEC cell setup. Anodic compartment for water photooxidation (left) and cathodic compartment for CO_2 reduction with immobilized catalyst **Co4** (right). Reproduced with permission from [80].

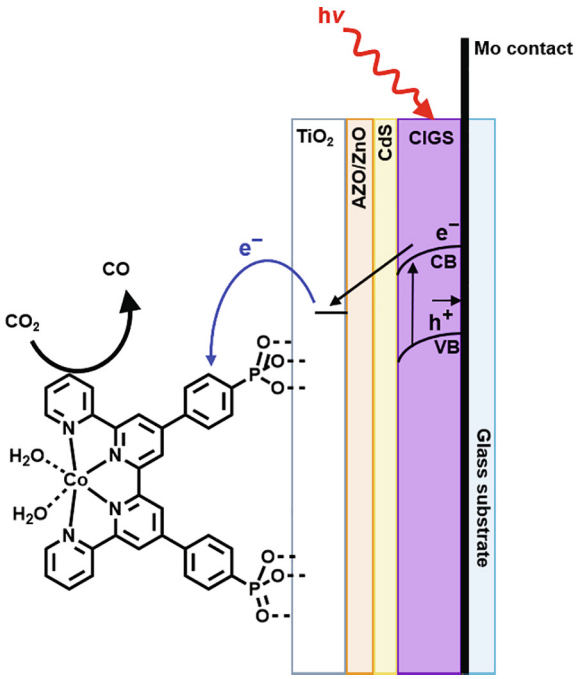

Fig. 24. A diagram of the CIGS photocathode functionalized for PEC CO_2 reduction with a phosphonated analogue of the **Co2** catalyst. Adapted from [81].

due to the lack of suitable *p*-type semiconductors and this consequently made the photoanode/cathode combination a more practical setup. Effective immobilization of the two fluorinated cobalt complexes was facilitated through non-covalent hydrophobic interactions with the (photo)electrodes which enabled the long term stability of the hybrid system in the aqueous environment. Photo-assisted controlled potential electrolysis of a $NaHCO_3$ aqueous solution (pH 8.15) was performed with the described PEC cell. CO and H_2 were detected as the major products of the cathodic compartment, while O_2 evolved from the photoanode. After 5 h of chopped illumination from a solar simulator (AM 1.5G, 100 mW/cm^2 simulated sunlight; stable photocurrent of 0.75 mA/cm^2) the TON_{CO} was 966 based on the amount of loaded **Co4**, with an initial evolution rate of 9.4 μmol h^{-1}. The faradic efficiency for CO production (defined as the ratio between the moles of evolved CO and the charge passed through the cell) reached the maximum value of 87% when a potential of 1.1 V was applied across the cell. This excellent selectivity for CO_2 reduction highlights the efficacy of the hybrid in suppressing the competing H_2 evolution.

A second noticeable example of heterogenized CO_2 catalysts in PEC system involves **Co2** quaterpyridine (qpy), which is a very efficient molecular catalyst for the CO_2-to-CO reduction and has been discussed earlier in this review [81]. In this PEC system, the qpy ligand was modified with two phosphonic acid groups to allow the catalyst to be grafted to a photocathode made of multiple layers. The outer layer was made of TiO_2 and **Co2** was anchored to this. Protective ZnO and ZnO:Al layers, a CdS buffer layer, a CIGS (copper indium gallium selenium) light-absorbing layer, a molybdenum back-contact layer, and finally the glass substrate were layered beneath the **Co2** modified-TiO_2 (Fig. 24). CIGS materials have high absorption in the visible range and their bandgaps are easily tunable through variation of the material composition (In/Ga ratio). Importantly, they can also be manufactured at low cost. Using CIGS as the PS is quite different to the DSPC system which uses molecular PSs. This example is almost analogous to the QD dispersions previously discussed, or the doped-TiO_2 particles. Linear sweep voltammetry of the CIGS/**Co2**@TiO_2 electrode under chopped illumination in a 3-electrode cell with $KHCO_3$ aqueous solution (pH 6.8) revealed a photo-response with an onset potential of 0.2 V *vs.* RHE. Photocurrents as high as 3 mA cm^{-2} could be obtained at a bias potential of *ca.* −0.1 V *vs.* RHE (which is equal to $E^0(CO_2/CO)$). Photoelectrocatalysis experiments at a bias potential of −0.06 V *vs.* RHE for 2 h gave an average current density for CO of 0.72 mA cm^{-2}. A slight decrease in photocurrent was observed and could be due to catalyst leaching from the electrode, or the instability of the different layers in aqueous environment. It corresponds to CO production with a TON of 8031 and a 97% selectivity after 2 h of visible light illumination (Faradaic efficiency = 89%; mean TOF_{CO} = 1.1 s^{-1}).

Recently, Reisner and co-workers reported a precious metal-free photocathode bearing a phosphonated Co^{II} terpyridine complex (**Co8**, Chart 1 and Fig. 25) [82]. The photoelectrochemical hybrid system consisted of a *p*-silicon photoelectrode coated with mesoporous TiO_2 onto which the cobalt catalyst was adsorbed. The light-harvesting function was performed by the Si layer, while the high-surface area titania provided protection for the silicon and enabled high loadings of the adsorbed complex to be achieved. Under illumination, the silicon was able to inject electrons into the titania, which then shuttled them to the anchored catalyst. UV–Vis spectroscopy confirms that the structure of **Co8** was preserved after grafting. When the photocathode was placed in an ACN solution with tetrabutylammonium tetrafluoroborate, no CO_2 reduction products could be detected. However, the addition

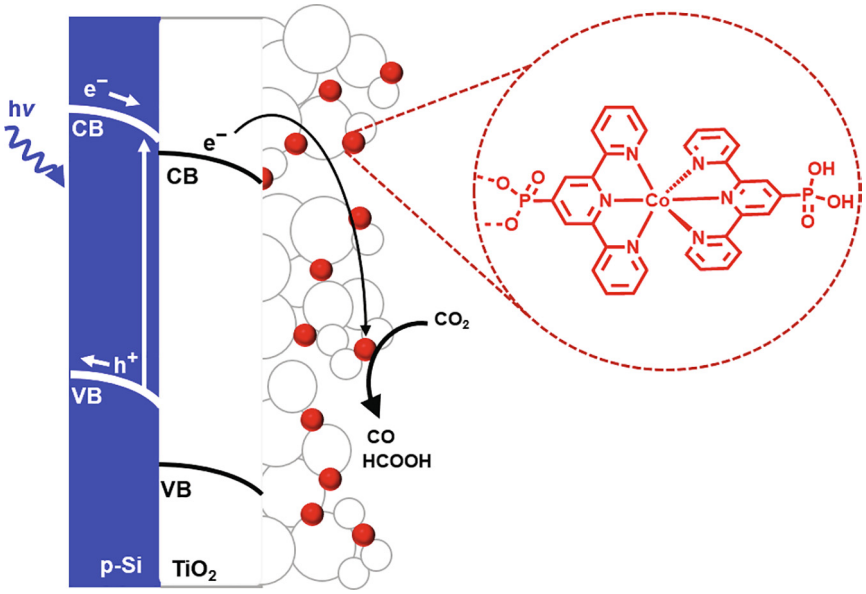

Fig. 25. Schematic representation of the hybrid system. Adapted from [82].

of an optimized amount of water (ACN:H_2O 6:4) led to the production of CO and formate with an overall TON of 159 and a Faradaic efficiency of 77% (8 h, λ > 400 nm) at an applied potential of −1.0 V *vs.* Fc^+/Fc. The photocathode maintained activity during 24 h of operation, albeit at a modest current density (<0.5 mA cm^{-2}). A TON_{CO} of 334 and a $TON_{formate}$ of 47 (53% selectivity toward CO_2 reduction) were achieved with this system. A gradual drop in Faradaic efficiency was observed which could be a result of progressive desorption of **Co8** (similar to the previous examples).

4. Concluding remarks

In summary, heterogenization of molecular CO_2 reduction catalysts has been successfully used to increase the stability of many photocatalytic systems. Also, the selectivity for CO_2 reduction over H_2 production appears to be increased in photocatalysis when hydrophobic supports are used [60,65]. Using co-anchored PSs, photoactive supports, or confining PSs close to molecular catalysts in MOFs have been used to increase the light harvesting efficiency of a number of heterogenized photochemical CO_2 reduction systems [58,60,63,66]. Specifically, new advances in MOF and COF chemistry have introduced new immobilization methods for CO_2 reduction catalysts, either through coordination into pores [70,71], or effectively polymerising molecular catalysts into large porous 3D, catalytic MOFs [47]. Interestingly, heterogenization of group 4 transition metal catalysts onto amorphous polymers is absent in recent photocatalytic CO_2 reduction research and has not transferred from closely related fields, such as photocatalytic water splitting. However, this may be because of an alternate focus on making metal-free polymer systems with inherent photocatalytic activity.

Colloidal dispersions of solid-supported catalysts in photocatalytic mixtures still require SDs which could be a hurdle to using these catalysts in sustainable industrial scale processes. To address this, the chemistry used to anchor molecular catalysts to inorganic and carbonaceous supports has been used to construct electrodes and photoelectrodes for PEC cells. This should eventually allow SDs such as TEA to be replaced by the more abundant and benign H_2O [80,81]. PEC devices for CO_2 reduction are in the very early stages of research. However, they benefit from building on decades of existing research on dye-sensitized solar cells and more recent water-splitting PEC development. In other fields, MOFs have been immobilized onto electrodes and this would be a logical next step for these materials. COFs have already been used to heterogenized molecular catalysts in electrolysis. An alternative to electrochemical cells for replacing SDs is single particle Z-scheme catalysis. In such systems, CO_2 is photo-reduced and water oxidized at the same catalytic particle/surface. The materials used for this are the same semi-conductors, carbon materials, and MOFs discussed here as support materials. However, molecular catalysts are as of yet to be thrown into the mix [83]. It is worth noting that if the schemes produce gaseous mixtures of oxygen and flammable CO_2 reduction products, this would provide an interesting separation challenge to allow scaling-up.

A wealth of structure–function knowledge exists for MOFS in chemical separation and gas absorption. This could be employed in the future to design materials with selective pores that prevent catalyst poisoning, change the composition of the product mixture, or perhaps separate gaseous mixtures. Some of this chemistry could also be translated to COFs. Finally, heterogenization of molecular catalysts that can produce multi-carbon products from CO_2 should be a goal for those aiming for solar fuels and feedstocks, or co-heterogenization of CO_2 photocatalysts with catalysts that generate multi-carbon products from CO_2 precursors.

Declaration of Competing Interest

The authors declare that they have no known competing financial interests or personal relationships that could have appeared to influence the work reported in this paper.

Acknowledgements

Financial support from the MARS consortium (GRDF, GRTgaz and Térega) to G. L. and partial financial support to M.R. from the Institut Universitaire de France (IUF) are gratefully acknowledged.

References

[1] M. Aresta, A. Dibenedetto, A. Angelini, Chem. Rev. 114 (2014) 1709–1742.
[2] A.J. Morris, G.J. Meyer, E. Fujita, Acc. Chem. Res. 42 (2009) 1983–1994.
[3] N. Elgrishi, S. Griveau, M.B. Chambers, F. Bedioui, M. Fontecave, Chem. Commun. 51 (2015) 2995–2998.

[4] C.D. Windle, E. Reisner, Chimia 69 (2015) 435–441.
[5] J.L. White, M.F. Baruch, J.E. Pander, Y. Hu, I.C. Fortmeyer, J.E. Park, T. Zhang, K. Liao, J. Gu, Y. Yan, T.W. Shaw, E. Abelev, A.B. Bocarsly, Chem. Rev. 115 (2015) 12888–12935.
[6] K.E. Dalle, J. Warnan, J.J. Leung, B. Reuillard, I.S. Karmel, E. Reisner, Chem. Rev. 119 (2019) 2752–2875.
[7] I.N. Levine (Ed.), Physical Chemistry, fifth ed., McGraw-Hill, Boston, 2001, p. 955.
[8] M. Vert, Y. Doi, K.-H. Hellwich, M. Hess, P. Hodge, P. Kubisa, M. Rinaudo, F. Schué, Pure Appl. Chem. 84 (2012) 377–410.
[9] J. Willkomm, K.L. Orchard, A. Reynal, E. Pastor, J.R. Durrant, E. Reisner, Chem. Soc. Rev. 45 (2016) 9–23.
[10] R.D. Harris, S. Bettis Homan, M. Kodaimati, C. He, A.B. Nepomnyashchii, N.K. Swenson, S. Lian, R. Calzada, E.A. Weiss, Chem. Rev. 116 (2016) 12865–12919.
[11] Y. Bao, J. Wang, Q. Wang, X. Cui, R. Long, Z. Li, Nanoscale 12 (2020) 2507–2514.
[12] M. Liu, M. Liu, X. Wang, S.M. Kozlov, Z. Cao, P. De Luna, H. Li, X. Qiu, K. Liu, J. Hu, C. Jia, P. Wang, H. Zhou, J. He, M. Zhong, X. Lan, Y. Zhou, Z. Wang, J. Li, A. Seifitokaldani, C.T. Dinh, H. Liang, C. Zou, D. Zhang, Y. Yang, T.-S. Chan, Y. Han, L. Cavallo, T.-K. Sham, B.-J. Hwang, E.H. Sargent, Joule 3 (2019) 1703–1718.
[13] H.-L. Wu, X.-B. Li, C.-H. Tung, L.-Z. Wu, Adv. Mater. 31 (2019) 1900709.
[14] H. Moon, C. Lee, W. Lee, J. Kim, H. Chae, Adv. Mater. 31 (2019) 1804294.
[15] F.K. Kessler, Y. Zheng, D. Schwarz, C. Merschjann, W. Schnick, X. Wang, M.J. Bojdys, Nat. Rev. Mater. 2 (2017) 17030.
[16] M.-Q. Yang, N. Zhang, M. Pagliaro, Y.-J. Xu, Chem. Soc. Rev. 43 (2014) 8240–8254.
[17] G.A.M. Hutton, B.C.M. Martindale, E. Reisner, Chem. Soc. Rev. 46 (2017) 6111–6123.
[18] R.S. Sprick, B. Bonillo, M. Sachs, R. Clowes, J.R. Durrant, D.J. Adams, A.I. Cooper, Chem. Commun. 52 (2016) 10008–10011.
[19] J.-H. Liu, Y. Wang, G.-H. Yan, F. Yang, H. Gao, Y. Huang, H. Wang, P. Wang, L. Yang, Y. Tang, L.R. Teisl, Y.-P. Sun, J. Nanosci. Nanotechnol. 19 (2019) 2130–2137.
[20] A. Thomas, A. Fischer, F. Goettmann, M. Antonietti, J.-O. Müller, R. Schlögl, J.M. Carlsson, J. Mater. Chem. 18 (2008) 4893–4908.
[21] J. Qin, S. Wang, H. Ren, Y. Hou, X. Wang, Applied Cat. B 179 (2015) 1–8.
[22] J. Lin, Z. Pan, X. Wang, ACS Sustainable Chem. Eng. 2 (2014) 353–358.
[23] E.A. Weiss, ACS Energy Lett. 2 (2017) 1005–1013.
[24] F. Lakadamyali, E. Reisner, Chem. Commun. 47 (2011) 1695–1697.
[25] C. Bachmann, B. Probst, M. Oberholzer, T. Fox, R. Alberto, Chem. Sci. 7 (2016) 436–445.
[26] J. Willkomm, N.M. Muresan, E. Reisner, Chem. Sci. 6 (2015) 2727–2736.
[27] J. Shamsi, A.S. Urban, M. Imran, L.D. Trizio, L. Manna, Chem. Rev. 119 (2019) 3196–3348.
[28] Q.A. Akkerman, G. Rainò, M.V. Kovalenko, L. Manna, Nat. Mat. 17 (2018) 394–405.
[29] M. Ou, W. Tu, S. Yin, W. Xing, S. Wu, H. Wang, S. Wan, Q. Zhong, R. Xu, Angew. Chem. Int. Ed. 57 (2018) 13570–13574.
[30] Y.-F. Xu, M.-Z. Yang, B.-X. Chen, X.-D. Wang, H.-Y. Chen, D.-B. Kuang, C.-Y. Su, J. Am. Chem. Soc. 139 (2017) 5660–5663.
[31] L.-Y. Wu, Y.-F. Mu, X.-X. Guo, W. Zhang, Z.-M. Zhang, M. Zhang, T.-B. Lu, Angew. Chem. Int. Ed. 58 (2019) 9491–9495.
[32] Z. Chen, Y. Hu, J. Wang, Q. Shen, Y. Zhang, C. Ding, Y. Bai, G. Jiang, Z. Li, N. Gaponik, Chem. Mater. 32 (2020) 1517–1525.
[33] M. Delamar, R. Hitmi, J. Pinson, J.M. Saveant, J. Am. Chem. Soc. 114 (1992) 5883–5884.
[34] P. Allongue, M. Delamar, B. Desbat, O. Fagebaume, R. Hitmi, J. Pinson, J.-M. Savéant, J. Am. Chem. Soc. 119 (1997) 201–207.
[35] S. Mahouche-Chergui, S. Gam-Derouich, C. Mangeney, M.M. Chehimi, Chem. Soc. Rev. 40 (2011) 4143–4166.
[36] N. Tagmatarchis, M. Prato, J. Mater. Chem. 14 (2004) 437–439.
[37] A. Devadoss, C.E.D. Chidsey, J. Am. Chem. Soc. 129 (2007) 5370–5371.
[38] Y.-L. Zhao, J.F. Stoddart, Acc. Chem. Res. 42 (2009) 1161–1171.
[39] P.D. Tran, A. Le Goff, J. Heidkamp, B. Jousselme, N. Guillet, S. Palacin, H. Dau, M. Fontecave, V. Artero, Angew. Chem. Int. Ed. 50 (2011) 1371–1374.
[40] S.P. Pujari, L. Scheres, A.T.M. Marcelis, H. Zuilhof, Angew. Chem. Int. Ed. 53 (2014) 6322–6356.
[41] B.J. Brennan, M.J. Llansola Portolés, P.A. Liddell, T.A. Moore, A.L. Moore, D. Gust, Phys. Chem. Chem. Phys. 15 (2013) 16605–16614.
[42] C. Queffélec, M. Petit, P. Janvier, D.A. Knight, B. Bujoli, Chem. Rev. 112 (2012) 3777–3807.
[43] W.R. McNamara, R.L. Milot, H.-E. Song, R.C. Snoeberger Iii, V.S. Batista, C.A. Schmuttenmaer, G.W. Brudvig, R.H. Crabtree, Energy Environ. Sci. 3 (2010) 917–923.
[44] T.P. Brewster, S.J. Konezny, S.W. Sheehan, L.A. Martini, C.A. Schmuttenmaer, V. S. Batista, R.H. Crabtree, Inorg. Chem. 52 (2013) 6752–6764.
[45] J. Warnan, Y. Pellegrin, E. Blart, L. Zhang, A. Brown, L. Hammarström, D. Jacquemin, F. Odobel, Dyes Pigm. 105 (2014) 174–179.
[46] P.R. Brown, D. Kim, R.R. Lunt, N. Zhao, M.G. Bawendi, J.C. Grossman, V. Bulović, ACS Nano 8 (2014) 5863–5872.
[47] S. Wang, W. Yao, J. Lin, Z. Ding, X. Wang, Angew. Chem. Int. Ed. 53 (2014) 1034–1038.
[48] P. Mialane, C. Mellot-Draznieks, P. Gairola, M. Duguet, Y. Benseghir, O. Oms, A. Dolbecq, Chem. Soc. Rev. (2021), Advance Article.
[49] K. Gottschling, G. Savasci, H. Vignolo-González, S. Schmidt, P. Mauker, T. Banerjee, P. Rovó, C. Ochsenfeld, B.V. Lotsch, J. Am. Chem. Soc. 142 (2020) 12146–12156.
[50] L. Grunenberg, G. Savasci, M.W. Terban, V. Duppel, I. Moudrakovski, M. Etter, R. E. Dinnebier, C. Ochsenfeld, B.V. Lotsch, J. Am. Chem. Soc. 143 (2021) 3430–3438.
[51] T. Inoue, A. Fujishima, S. Konishi, K. Honda, Nature 277 (1979) 637–638.
[52] G. Zhao, H. Pang, G. Liu, P. Li, H. Liu, H. Zhang, L. Shi, J. Ye, Appl. Catal. B 200 (2017) 141–149.
[53] K. Maeda, Adv. Mater. 31 (2019) 1808205.
[54] S. Tian, S. Chen, X. Ren, Y. Hu, H. Hu, J. Sun, F. Bai, Nano Res. 13 (2020) 2665–2672.
[55] L. Lin, C. Hou, X. Zhang, Y. Wang, Y. Chen, T. He, Appl. Catal. B 221 (2018) 312–319.
[56] X. Zhang, L. Lin, D. Qu, J. Yang, Y. Weng, Z. Wang, Z. Sun, Y. Chen, T. He, Appl. Catal. B 265 (2020) 118595.
[57] S. Roy, E. Reisner, Angew. Chem. Int. Ed. 58 (2019) 12180–12184.
[58] B. Ma, G. Chen, C. Fave, L. Chen, R. Kuriki, K. Maeda, O. Ishitani, T.-C. Lau, J. Bonin, M. Robert, J. Am. Chem. Soc. 142 (2020) 6188–6195.
[59] C. Cometto, R. Kuriki, L. Chen, K. Maeda, T.-C. Lau, O. Ishitani, M. Robert, J. Am. Chem. Soc. 140 (2018) 7437–7440.
[60] S. Aoi, K. Mase, K. Ohkubo, S. Fukuzumi, Catal. Sci. Technol. 6 (2016) 4077–4080.
[61] M.F. Kuehnel, K.L. Orchard, K.E. Dalle, E. Reisner, J. Am. Chem. Soc. 139 (2017) 7217–7223.
[62] Q.-Q. Bi, J.-W. Wang, J.-X. Lv, J. Wang, W. Zhang, T.-B. Lu, ACS Catal. 8 (2018) 11815–11821.
[63] S. Lian, M.S. Kodaimati, D.S. Dolzhnikov, R. Calzada, E.A. Weiss, J. Am. Chem. Soc. 139 (2017) 8931–8938.
[64] S. Lian, M.S. Kodaimati, E.A. Weiss, ACS Nano 12 (2018) 568–575.
[65] M.F. Kuehnel, C.D. Sahm, G. Neri, J.R. Lee, K.L. Orchard, A.J. Cowan, E. Reisner, Chem. Sci. 9 (2018) 2501–2509.
[66] T. Jin, C. Liu, G. Li, Chem. Commun. 50 (2014) 6221–6224.
[67] S.-J. Woo, S. Choi, S.-Y. Kim, P.S. Kim, J.H. Jo, C.H. Kim, H.-J. Son, C. Pac, S.O. Kang, ACS Catal. 9 (2019) 2580–2593.
[68] T.W. Woolerton, S. Sheard, E. Pierce, S.W. Ragsdale, F.A. Armstrong, Energy Environ. Sci. 4 (2011) 2393–2399.
[69] G. Neri, M. Forster, J.J. Walsh, C.M. Robertson, T.J. Whittles, P. Farràs, A.J. Cowan, Chem. Commun. 52 (2016) 14200–14203.
[70] H. Fei, M.D. Sampson, Y. Lee, C.P. Kubiak, S.M. Cohen, Inorg. Chem. 54 (2015) 6821–6828.
[71] M. Lu, Q. Li, J. Liu, F.-M. Zhang, L. Zhang, J.-L. Wang, Z.-H. Kang, Y.-Q. Lan, Applied Cat. B 254 (2019) 624–633.
[72] T. Ouyang, H.-H. Huang, J.-W. Wang, D.-C. Zhong, T.-B. Lu, Angew. Chem. Int. Ed. 56 (2017) 738–743.
[73] G. Neri, J.J. Walsh, C. Wilson, A. Reynal, J.Y.C. Lim, X. Li, A.J.P. White, N.J. Long, J. R. Durrant, A.J. Cowan, Phys. Chem. Chem. Phys. 17 (2015) 1562–1566.
[74] D. Wang, R. Huang, W. Liu, D. Sun, Z. Li, ACS Catal. 4 (2014) 4254–4260.
[75] D. Sun, Y. Fu, W. Liu, L. Ye, D. Wang, L. Yang, X. Fu, Z. Li, Chem.– Eur. J. 19 (2013) 14279–14285.
[76] J. Jin, React. Kinet. Mech. Catal. 131 (2020) 397–408.
[77] S. Lin, C.S. Diercks, Y.-B. Zhang, N. Kornienko, E.M. Nichols, Y. Zhao, A.R. Paris, D. Kim, P. Yang, O.M. Yaghi, C.J. Chang, Science 349 (2015) 1208–1213.
[78] S. Guo, H. Zhang, Y. Chen, Z. Liu, B. Yu, Y. Zhao, Z. Yang, B. Han, Z. Liu, ACS Catal. 8 (2018) 4576–4581.
[79] K. Kamada, J. Jung, T. Wakabayashi, K. Sekizawa, S. Sato, T. Morikawa, S. Fukuzumi, S. Saito, J. Am. Chem. Soc. 142 (2020) 10261–10266.
[80] Y. Wang, Y. Zhu, L. Sun, F. Li, ACS Appl. Mater. Interfaces 12 (2020) 41644–41648.
[81] P.B. Pati, R. Wang, E. Boutin, S. Diring, S. Jobic, N. Barreau, F. Odobel, M. Robert, Nat. Commun. 11 (2020) 3499.
[82] J.J. Leung, J. Warnan, K.H. Ly, N. Heidary, D.H. Nam, M.F. Kuehnel, E. Reisner, Nat. Catal. 2 (2019) 354–365.
[83] W. Zhang, A.R. Mohamed, W.-J. Ong, Angew. Chem. Int. Ed. 59 (2020) 22894–22915.